Ore Geology Reviews 86 (2017) 35–54

Contents lists available at ScienceDirect

Ore Geology Reviews

journal homepage: www.elsevier.com/locate/oregeo

Zircon U-Pb geochronology and geochemistry of the intrusions associated with the Jiawula Ag-Pb-Zn deposit in the Great Xing'an Range, NE China and their implications for mineralization

Si-Da Niu [a,b], Sheng-Rong Li [a,b,*], Jan Marten Huizenga [c,d], M. Santosh [e,b], De-Hui Zhang [b], Yong-Jie Zeng [a,b], Zeng-Da Li [b], Wen-Bin Zhao [f]

[a] State Key Laboratory of Geological Processes and Mineral Resources, China University of Geosciences, Beijing 100083, China
[b] School of Earth Science and Resources, China University of Geosciences, Beijing 100083, China
[c] Economic Geology Research Institute (EGRU), College of Science and Engineering, James Cook University, QLD 4811, Australia
[d] Department of Geology, University of Johannesburg, Auckland Park, Johannesburg 2006, South Africa
[e] Department of Earth Sciences, University of Adelaide, SA 5005, Australia
[f] Xin Barag Right Banner Rongda Mining Limited Liability Company, Hulun Buir 021300, Inner Mongolia, China

ARTICLE INFO

Article history:
Received 30 August 2016
Received in revised form 3 February 2017
Accepted 6 February 2017
Available online 8 February 2017

Keywords:
SHRIMP U-Pb dating
Geochemistry
Sr-Nd isotopes
Jiawula deposit
Great Xing'an Range
Pb-Zn mineralization

ABSTRACT

Located in the eastern section of the Central Asian Orogenic Belt, the Jiawula Ag-Pb-Zn deposit is classified as a volcanic to subvolcanic related vein-type ore deposit. New U-Pb zircon geochronology, whole-rock geochemistry, mineral chemistry, and Sr-Nd isotope data are presented for the intrusions in the Jiawula deposit in order to evaluate the timing, petrogenetic type of the granitoid rocks, origin and evolution of magmatism, geodynamics, and to establish its relationship with lead-zinc mineralization. Zircon SHRIMP U-Pb analyses yield weighted mean ages of 150.1 ± 1.8 Ma for quartz porphyry, 148.8 ± 2.2 Ma for syenite porphyry, and 145.3 ± 1.9 Ma for monzonite porphyry, indicating a Late Jurassic (Yanshanian) magmatic event. An earlier magmatic event (Indosinian) occurred during the Late Permian to Early Triassic from ca. 254 Ma to ca. 247 Ma and is represented by granodiorite (254 ± 2 Ma), dacite porphyry (252.9 ± 4.8 Ma), and diorite porphyry (278 ± 4.1 Ma). Both the Indosinian and Yanshanian igneous rocks are classified as I-type granitoids. The late Jurassic intrusions are highly fractionated and characterized by negative anomalies of Eu, Sr, P, and Ti. The hypabyssal intrusions have initial $^{87}Sr/^{86}Sr$ values between 0.70458 and 0.70522, and $\varepsilon_{Nd}(t)$ values of −3.4 to −0.2, indicating relatively older crust in Jiawula among more juvenile crust in this area. Magma generation in Jiawula is linked to juvenile lower crustal and slightly enriched mantle sources. The ~250 Ma magmatic episode in Jiawula might be related to the subduction of the Mongol-Okhotsk oceanic plate towards the south beneath the Erguna massif. The ~150 Ma magmatic event occurred after the closure of the Mongol-Okhotsk Ocean followed by the change in subduction direction of the Paleo-Pacific plate. Varying temperature, stronger fractionation and higher oxygen fugacity related to the magmatic-hydrothermal transition caused Pb-Zn mineralization.

1. Introduction

The Great Xing'an Range in NE China forms an important part of the easternmost segment of the Central Asian Orogenic Belt (CAOB) and is characterized by numerous voluminous intrusions (Meng, 2003; Meng et al., 2011; Zhang et al., 2010, 2011; Wu et al., 2005, 2011). Recent geochronology data indicate that most of these intrusions were emplaced in Mesozoic (Wu et al., 2011; Ouyang et al., 2013; Wang et al., 2015; Tang et al., 2016).

The Great Xing'an Range is an important polymetallic metallogenic belt in northeastern China and hosts different types of Mesozoic base and precious metal mineral deposits, including porphyry, skarn, hydrothermal vein, and epithermal type deposits (Chen et al., 2012; Pirajno, 2012; Zhai et al., 2012; Liu et al., 2014). Geochronology indicates that mineralization in this region formed during the Late Mesozoic and peaked during the Early Cretaceous (Mao et al., 2003, 2013; Ouyang et al., 2013; Bai et al., 2014; Zhou et al., 2009, 2010, 2015). Most deposits appear to be closely associated with Mesozoic magmatic-hydrothermal activity.

* Corresponding author at: State Key Laboratory of Geological Processes and Mineral Resources, China University of Geosciences, Beijing 100083, China.
E-mail address: lisr@cugb.edu.cn (S.-R. Li).

http://dx.doi.org/10.1016/j.oregeorev.2017.02.007
0169-1368/

Previous studies have demonstrated that the Jiawula Ag-Pb-Zn deposit can be characterized as a volcanic-subvolcanic related hydrothermal vein deposit, which is transitional to mesothermal and epithermal types (Wu et al., 2006; Pirajno et al., 2009; Zhai et al., 2013). With proven reserves of 28 Mt of ore including about 1 Mt of lead, 1 Mt of zinc and 3106 t of silver, the Jiawula Ag-Pb-Zn deposit as well as adjacent Chagan Ag-polymetallic deposit have been regarded as important ore deposits, showing great metallogenic potential (Zhai et al., 2013). The porphyritic intrusions in Jiawula have a close spatial relationship with the mineralization.

A better understanding of the magmatic processes and the petrogenesis of the Jiawula intrusions can provide important clues on the geodynamic processes and the modifications in the lithospheric architecture over time (e.g. Li et al., 2014a; Li and Santosh, 2014; Guo et al., 2014; Sun et al., 2014; Zhang et al., 2015a). However, the precise ages of these intrusions have not been constrained and the temporal framework of magmatic-tectonic events is still ambiguous. In addition, the lack of information on the timing, petrogenesis, magma source and evolution of the Jiawula intrusions is a major limitation on understanding the relationship between magmatism and mineralization.

In this study, we present new data on SHRIMP zircon U-Pb geochronology, whole-rock geochemistry, mineral chemistry (EPMA), and Sr-Nd-Pb isotopes from a suite of magmatic intrusions in the Jiawula deposit. Based on the results, we discuss the timing and petrogenesis of the intrusions in order to establish the origin and evolution of magmatism, its geodynamic environment, and its relationship with lead–zinc mineralization in this area.

2. Regional geology

The Jiawula deposit is located in the western part of the great Xing'an Range within the eastern segment of the Central Asian Orogenic Belt (CAOB). The CAOB is a well-known Paleozoic orogenic collage between the Siberian Craton in the north and the Tarim and North China Cratons in the south (Fig. 1a) (Xiao et al., 2015 and references therein). The Jiawula deposit occurs in the southern part of the Erguna Block and to the NW of the Derbugan fault (Fig. 1b).

Several NE-SW striking faults have been identified in NE China, which separates this region into several tectonic blocks including

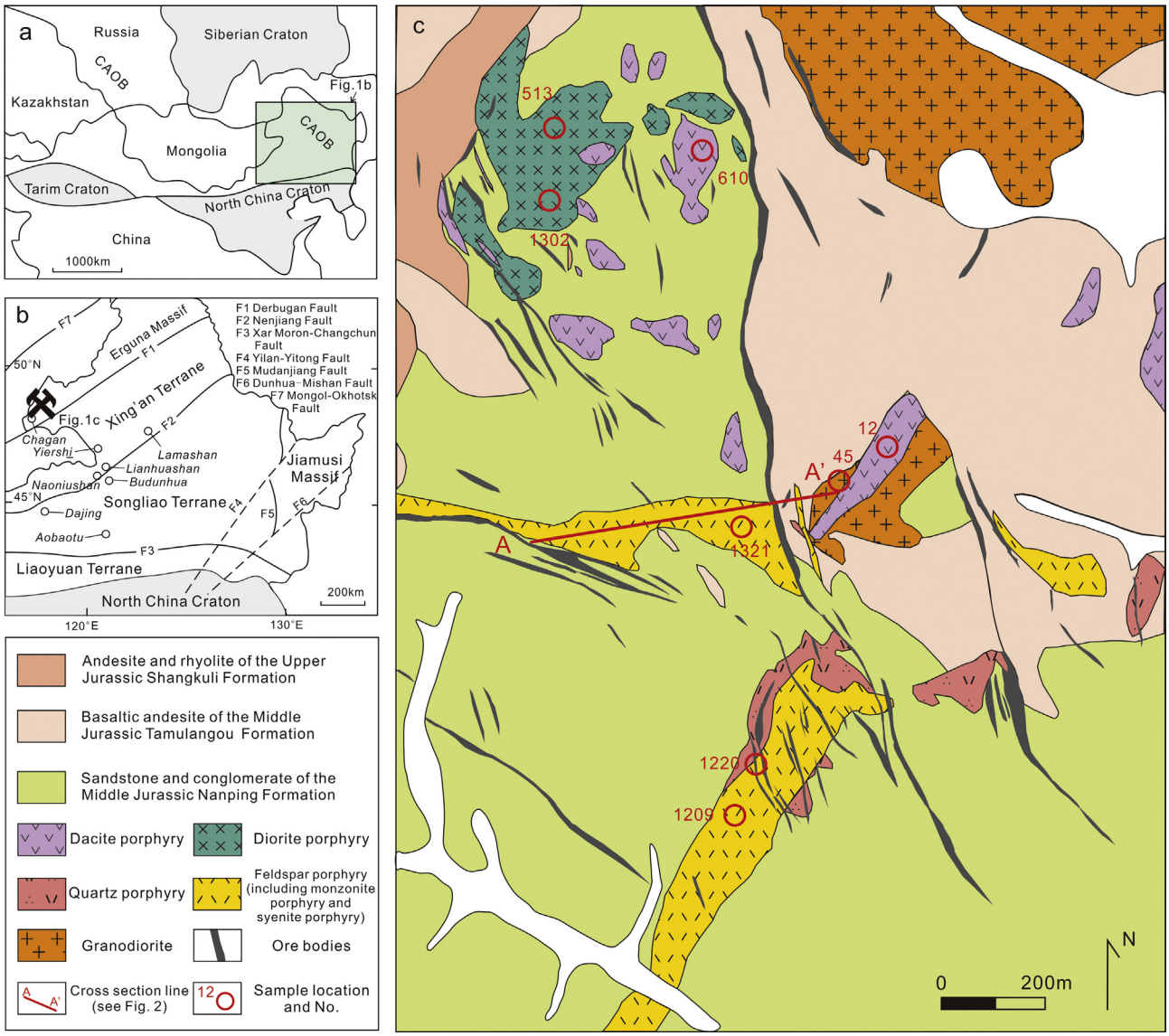

Fig. 1. (a) Location of the Central Asian Orogenic Belt in relation to the Siberian and North China Cratons (modified after Wu et al., 2011); (b) Regional geological setting of the Jiawula Deposit (modified after Wu et al., 2011); (c) Detailed geological map of the Jiawula deposit (modified after the geological map from mining company).

the Erguna block in the northwest, the Xing'an and Songliao blocks in the center, the Liaoyuan terrane in the southeast, and the Jiamusi massif in the east (Fig. 1b). The Erguna, Xing'an, and Songliao blocks are considered to form the eastern part of the CAOB, which amalgamated during the Paleozoic, whereas the Jiamusi massif comprises Early Mesozoic circum-Pacific accreted terranes (Wu et al., 2011). The Early-Middle Jurassic magmatic events are related to the subduction-related closure of the Mongol-Okhotsk Ocean to the Xing'an Mongolia Orogenic Belt, whereas the combined effects of the closure of the Mongol-Okhotsk Ocean (Yang et al., 2015; Tang et al., 2016) and the subduction of the Paleo-Pacific Oceanic plate may have been responsible for the large-scale magmatism and associated mineralization (Ouyang et al., 2013; Porter, 2016).

Two major tectono-stratigraphic units have been recognized in this region: (1) a pre-Jurassic metamorphic massif including quartzite and slate, and (2) a Mesozoic volcano-sedimentary sequence composed of basalt, andesite, and tuffaceous sandstone. The pre-Jurassic metamorphic massif is unconformably overlain by Late Jurassic to Early Cretaceous volcano-sedimentary sequences (Nie et al., 2015). The local stratigraphy of the Great Xing'an Range region is dominated by Jurassic successions and to a lesser extent by Cretaceous rocks (Zhai et al., 2013). The Jurassic rocks are mainly composed of carbonaceous mudstone (slate), siltstone, sandstone, and conglomerate of the Nanping Formation, and andesite, basaltic andesite, and minor pyroclastic rocks of the Tamulangou Formation.

Widespread magmatism in the form of multi-phase plutonic and volcanic activities took place across the Great Xing'an Range. Mafic-ultramafic rocks mainly formed in the Late Paleozoic and are mostly developed along the boundaries between the blocks. Massive intermediate-felsic intrusions were emplaced in the Late Paleozoic and Mesozoic (Liu et al., 2004). The Erguna Block shows evidence for four stages of granitic magmatism: Neoproterozoic (851–737 Ma), Early Paleozoic (ca. 490 Ma), Early-Middle Jurassic (200–160 Ma), and Early Cretaceous (ca. 130 Ma). The Neoproterozoic and Early Paleozoic granitoids occur scattered within the widespread Triassic-Jurassic plutons that range in age from 241 to 182 Ma (Wu et al., 2011; She et al., 2012; Tang et al., 2013; Ouyang et al., 2013).

Mesozoic magmatism shows a close temporal-spatial relationship with mineralization. Igneous bodies were emplaced in a shallow crustal setting as mid-hypabyssal, hypabyssal and ultra-hypabyssal intrusions of felsic and intermediate composition. The main rock assemblages include dacite porphyry, granite porphyry, quartz porphyry, and quartz monzonite porphyry (Zhai et al., 2013; Nie et al., 2015).

3. Geology of the Jiawula deposit

The Jiawula deposit occurs 45 km northwest of Xin Barag Right Banner and 150 km southwest from Manzhouli City (coordinates E

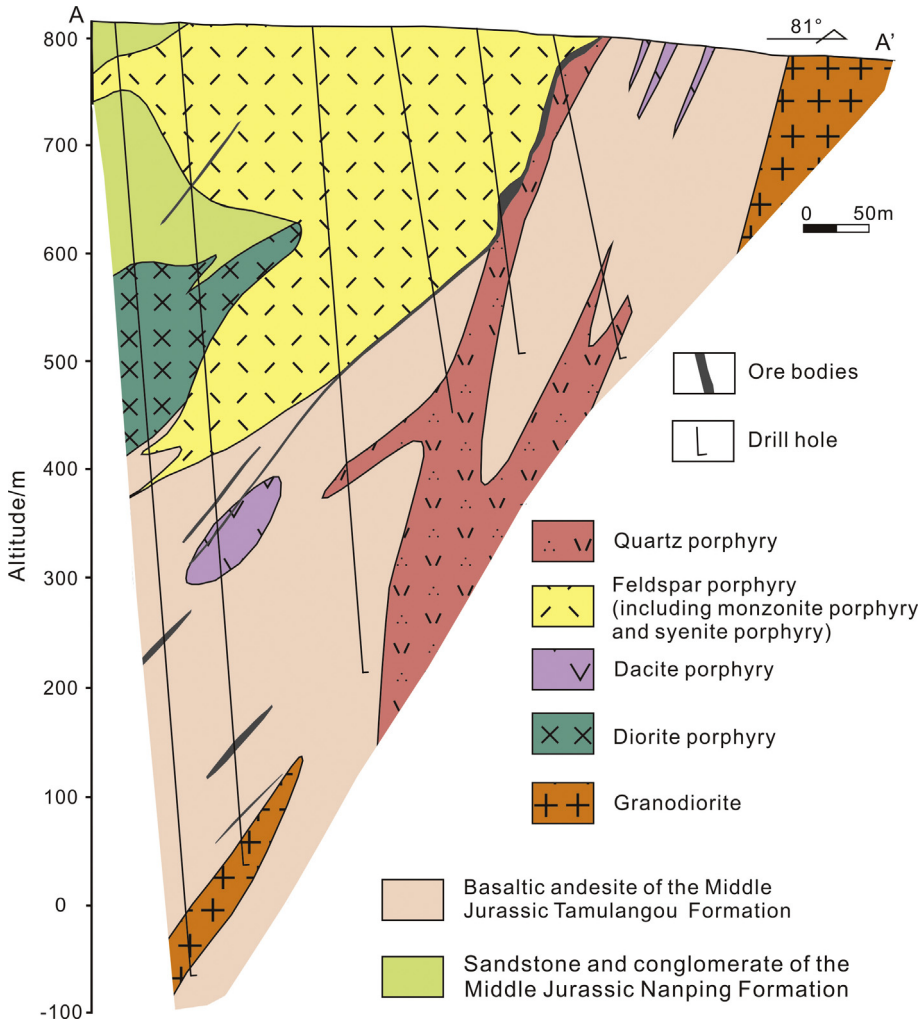

Fig. 2. Cross section of the Jiawula deposit (location of the section is shown on Fig. 1c).

116°14′30″–116°20′00″, N 48°46′00″–48°49′30″). The stratigraphy is dominated by Jurassic successions, composed of Middle Jurassic sandstone and conglomerate of the Nanping Formation, andesite and basaltic andesite of the Tamulangou Formation, and andesite and rhyolite of the Shangkuli Formation. Most of the ores are hosted by Jurassic rocks of the Tamulangou and Nanping Formations (Fig. 1c).

Northwest- and north-northwest-trending faults expand northwestward and converge to the southeast. Ore bodies are controlled by these faults, which have a genetic relationship with the volcanic edifice (Li et al., 2014b). The intrusions in the Jiawula deposit are mainly composed of Indosinian granite and granodiorite as well as late Yanshanian syenite porphyry, quartz porphyry and quartz monzonite porphyry. The mineralization of the Jiawula Ag-Pb-Zn deposit is spatially associated with the late Yanshanian intrusions. The quartz monzonite porphyry, which is associated with the mineralization, shows a single-grain zircon U-Pb age of 139.2 ± 0.5 Ma (Qin et al., 1996). The Rb-Sr isochron age of quartz in the Pb-Zn ore constrained as 140.0 ± 11.0 Ma (Wang et al., 2010) and the Rb-Sr isochron age from sphalerite and pyrite at 142.7 ± 1.3 Ma (Li et al., 2014b) mark the Early Cretaceous mineralization event.

More than 40 ore bodies have been identified in the Jiawula Ag-Pb-Zn deposit, most of which occur as veins. They occur in close proximity to the feldspar- and quartz porphyry intrusions, in fracture zones, or along the formation boundaries. The main ore minerals are pyrite, sphalerite, galena, chalcopyrite, arsenopyrite, and magnetite. Discrete grains of silver minerals (including argentite, pyrargyrite, and canfieldite) and isomorphism in silver-bearing sulfides are identified (Niu et al., 2016). Quartz, chlorite, calcite, rhodochrosite, muscovite, and fluorite are the main gangue

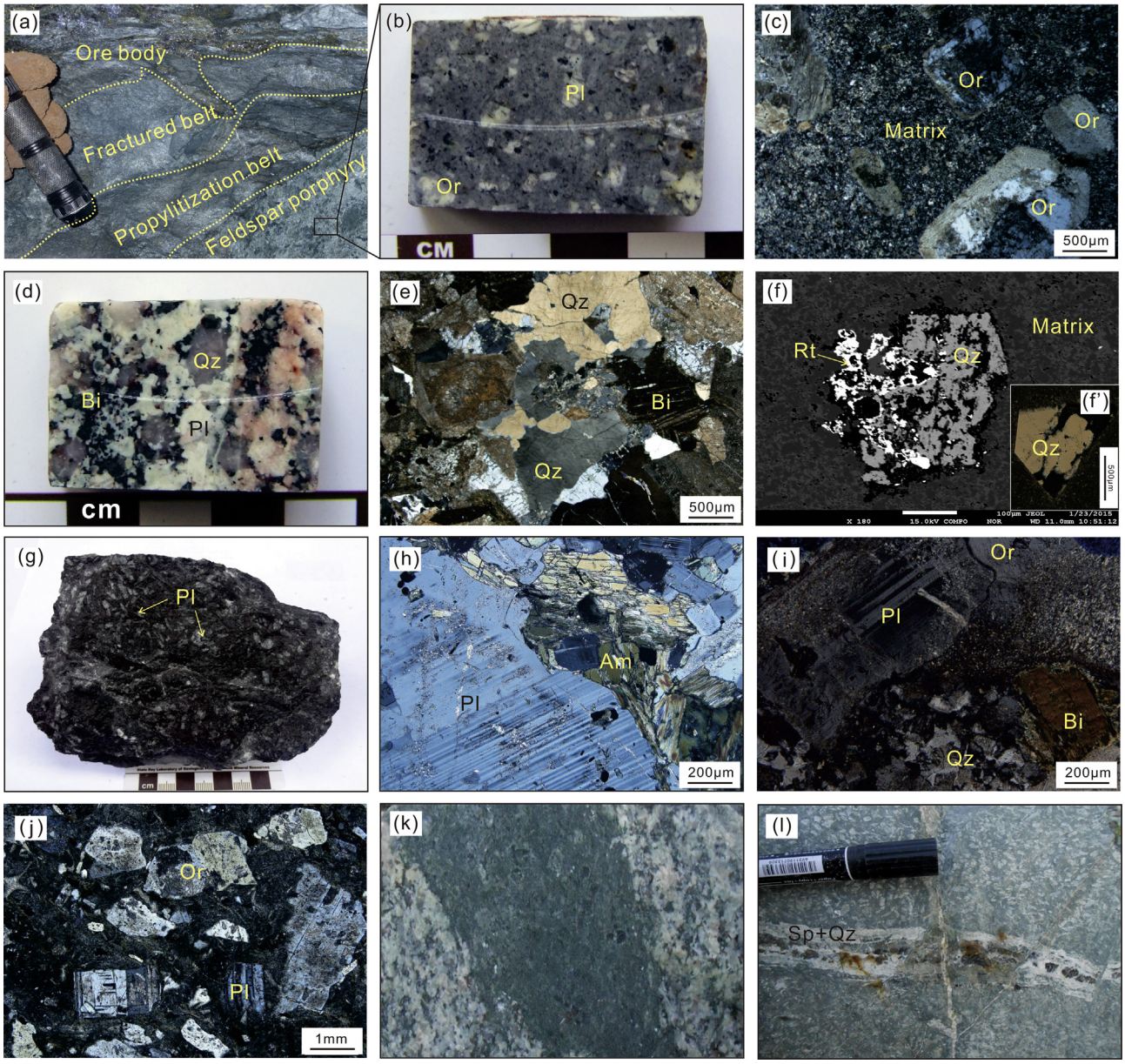

Fig. 3. Representative hand specimens and thin section photomicrographs of the igneous rocks of the Jiawula Ag-Pb-Zn deposit. (a) alteration zoning between the ore body and intrusions; (b) hand specimen of monzonite porphyry; (c) syenite porphyry showing mainly orthoclase phenocrysts (crossed polarized light); (d) granodiorite showing K-feldspar alteration; (e) granodiorite (crossed polarized light); (f) quartz phenocryst in quartz porphyry (crossed polarized light), the presence of rutile is shown in the backscattered electron image (f'). (g) diorite-porphyry with dominantly plagioclase and amphibole phenocrysts; (h) diorite porphyry (crossed polarized light); (i) dacite porphyry (crossed polarized light); (j) dacite porphyry (crossed polarized light); (k) diorite vein with propylitization cuts granodiorite; (l) diorite porphyry cut by sphalerite and quartz vein. Or: orthoclase; Pl: plagioclase; Qz: quartz; Bi: biotite; Rt: rutile; Am: amphibole; Sp: sphalerite.

minerals. The ores show vein, vein networks, disseminated, banded, and massive structures. Idiomorphic or hypidiomorphic, and xenomorphic textures are common. Replacement and exsolution textures are also commonly present. The Jiawula deposit shows an alteration zonation from a core of quartz-sericite-pyrite to actinolite-sericite-epidote to epidote-carbonate-chlorite at the margins (Pan and Sun, 1992; Pirajno et al., 2009; Zhai et al., 2013; Fig. 3a).

4. Sampling and analytical techniques

4.1. Sample description

The major intrusive rocks in the Jiawula deposit include monzonite porphyry, syenite porphyry, quartz porphyry, dacite porphyry, diorite porphyry, and granodiorite. Representative samples (see Fig. 1c for sample localities) were selected for zircon dating, whole-rock, mineral and Sr-Nd-Pb isotope geochemical studies.

The feldspar porphyry and quartz porphyry are closely related to the ore bodies (Fig. 2). The phenocrysts in the monzonite porphyry (0.3–0.8 cm in size) are mainly made up of K-feldspar (35–40 vol%), plagioclase (35–40 vol%), biotite (5–10 vol%), and hornblende (5–10 vol%) (Fig. 3b). The syenite porphyry comprises K-feldspar (75–80 vol%) and biotite (15–20 vol%) phenocrysts (0.3–0.5 cm in size). Quartz and K-feldspar can be identified in the matrix (Fig. 3c). The quartz porphyry shows a faint yellow color with porphyritic texture in hand specimen. The rock is composed of quartz phenocrysts (0.2–2 mm in size) and a quartz-K-feldspar matrix. Backscattered electron imaging demonstrates that rutile is occasionally associated with quartz phenocrysts in the quartz porphyry (Fig. 3f).

The granodiorite is coarse grained and comprises plagioclase (25–30 vol%), K-feldspar (15–20 vol%), quartz (15–20 vol%), hornblende (10–15 vol%), and biotite (10–15 vol%) (Fig. 3d and e). Apatite and zircon occur as accessory minerals in this rock. The porphyritic gray-green diorite porphyry comprises amphibole (30–35 vol%), plagioclase (55–60 vol%),±biotite (up to 5 vol%) phenocrysts (0.2 mm to 0.6 cm in size) (Fig. 3g and h). Apatite occurs as an accessory mineral; quartz, plagioclase, and hornblende form the matrix. The phenocrysts in the dacite porphyry include plagioclase (40–45 vol%), K-feldspar (35–40 vol%), and minor biotite (5–10 vol%) and quartz (5 vol%) (Fig. 3i and j). The matrix is composed of quartz and feldspar.

4.2. Analytical techniques

Whole-rock geochemistry was done at the Beijing Research institute of Uranium Geology, China. Major element oxides were analyzed using a Panalytical PW4400 X-ray fluorescence spectrometer (analytical accuracy: 0.01 wt%). The GB/T14506.28 standard was used for Na_2O, MgO, Al_2O_3, SiO_2, P_2O_5, K_2O, CaO, TiO_2, MnO, and Fe_2O_3 whereas the GB/T14506.28 and LY/T1253-1999 standards were used for FeO and LOI, respectively. Trace elements including REEs were analyzed using an X-series plasma mass spectrometer with reference to the DZ/T0223-2001 standard (analytical accuracy: 0.1 ppm).

The major and minor element compositions of minerals in this study were determined at the Chinese Academy of Geological Sciences, using a JEOL JXA-8230 electron microprobe. Operating conditions for minerals except for quartz were 15 kV accelerating voltage, a beam current of 20 nA, counting time of 10 s (peak position), and a beam diameter of 5 μm (analytical accuracy: 0.01 wt%). A high current of >100 nA, combined with a counting time of 30 up to 200 s for Ti (accuracy: 0.001 wt%), was used for quartz.

Zircon separation was performed at Langfang Regional Geological Survey in Hebei, China. Zircon crystals were extracted by magnetic and density methods after crushing, then hand-picked under a binocular microscope, mounted onto an epoxy resin disk and polished. After preparation of the mount, all zircon grains were microscopically examined under transmitted and reflected light. Zircon internal textures were studied by cathodeluminescence using a microprobe at the Beijing SHRIMP Center.

The SHRIMP analyses were performed on the SHRIMP II ion microprobe at Curtin University. The mass resolution used to measure Pb/Pb and Pb/U mass ratios was ~5000 (1%) during two analytical sessions. Mass ratios were normalized to those measured on the standard Sri Lankan gem zircon CZ3 ($^{206}Pb/^{238}U = 0.0914$). Uncertainties on individual analyses are based mainly on counting statistics and are reported at the 1σ level. Errors on pooled analyses are reported at 2σ (95% confidence).

Sr and Nd isotopic analyses were performed at the Beijing Research Institute of Uranium Geology. The Sr–Nd isotopic measurements were made by an ISOPROBE-T multi-collector thermal ionization mass spectrometer. The $^{87}Sr/^{86}Sr$ ratio of the NBS987 standard and $^{143}Nd/^{144}Nd$ ratio of the SHINESTU standard were 0.71025 ± 7 (2σ) 256 and 0.512118 ± 3 (2σ), respectively. The measurement accuracy of the Rb/Sr mass ratio was better than 0.1%. The mass fractionation of Sr isotopes was corrected using $^{86}Sr/^{88}Sr = 0.1194$. The accuracy of the Sm/Nd mass ratio was better than 0.1% and the mass fractionation of Nd isotopes was corrected using $^{146}Nd/^{144}Nd = 0.7219$. The $^{87}Rb/^{86}Sr$ and $^{147}Sm/^{144}Nd$ ratios were calculated using the Rb, Sr, Sm, and Nd abundances measured by ICP-MS.

5. Analytical results

5.1. Whole-rock major and trace elements

Whole-rock major and trace element data of the representative samples from Jiawula and other intrusions from the Great Xing'an Range area are presented in Tables 1 and 2. The Indosinian Group has lower content of SiO_2 (59.1–66.6 wt%), K_2O (1.75–4.61 wt%), and higher contents of Al_2O_3 (14.7–16.8 wt%), CaO (0.78–3.70 wt%), MgO (1.62–3.58 wt%), Fe_2O_3 (total) (4.92–6.68 wt%), TiO_2 (0.75–0.95 wt%) and P_2O_5 (0.18–0.27 wt%), compared to the Yanshanian Group with the contents of SiO_2 (68.1–77.5 wt%), K_2O (5.02–6.80 wt%), Al_2O_3 (12.4–14.9 wt%), CaO (0.08–1.28 wt%), MgO (0.27–0.75 wt%), Fe_2O_3 (total) (0.53–2.89 wt%), TiO_2 (0.13–0.52 wt%) and P_2O_5 (0.02–0.15 wt%). The Na_2O content of the Indosinian and Yanshannian group varies between 2.86 and 4.79 wt%, and 0.19 and 4.18 wt%, respectively. The MnO content is not greater than 0.2 wt% in all analyzed samples.

The Yanshanian intrusions that are temporally linked to mineralization and emplaced in Late Jurassic, show calc-alkaline, medium to high K, and peraluminous characteristics. The Indosinian intrusions display calc-alkaline, high K, and peraluminous features (TAS and AFM diagrams shown in Fig. 4). Harker diagrams (Fig. 5) reveal that Al_2O_3, CaO, MgO, Fe_2O_3 (total), Na_2O, Ti_2O, P_2O_5 correlate negatively with SiO_2, suggesting possible fractional crystallization. MnO and Na_2O do not show a significant correlation with SiO_2. These data reflect the difference in metallogenic specialization among various mineralization series in the Great Xing'an Range.

Chondrite-normalized REE patterns (normalization values after Sun and McDonough, 1989) for the Early Cretaceous Jiawula intrusions show enrichment in light rare earth elements (LREE) relative to the heavy rare earth elements (HREE) with LREE/HREE ratios of 8.12–11.59. The Indosinian Group shows weak Eu negative anomalies ($Eu/Eu* = 0.68–0.80$) whereas the late Yanshanian Group displays strong negative Eu anomalies ($Eu/Eu* = 0.15–0.40$) (Fig. 6a). The Indosinian Group is characterized by the depletion of Ta, Nb, P, Ti in and Sr (Fig. 6b). Rocks of the Yanshanian Group, on the other hand, show stronger depletion of Sr, Ti, and P, and a negative

Table 1
Whole-rock geochemical data of the intrusions from the Jiawula deposit.

Sample	45	12	1302	1209	1321	1220
Major oxides (wt.%)						
SiO_2	62.52	66.63	59.08	69.29	68.08	77.47
Al_2O_3	16.76	14.66	15.73	14.73	14.86	12.42
TFe_2O_3	4.92	5.12	6.68	2.38	2.89	0.532
MgO	1.62	1.47	3.58	0.626	0.748	0.268
CaO	2.49	0.775	3.7	1.24	1.28	0.082
Na_2O	4.79	2.86	4.33	4.18	4.17	0.192
K_2O	2.65	4.61	1.75	5.02	5.24	6.8
MnO	0.121	0.139	0.096	0.122	0.069	0.011
TiO_2	0.752	0.626	0.953	0.458	0.524	0.134
P_2O_5	0.237	0.177	0.273	0.105	0.146	0.022
LOI	3.12	2.34	3.82	1.83	1.47	1.55
Total	99.98	99.41	99.99	99.98	99.48	99.48
$Mg^{\#}$	25	22	35	21	21	34
FeO	3.01	4.27	4.42	1.79	2.36	0.44
Trace elements (ppm)						
B	16.6	7.54	11.4	10.4	7.88	27.3
Li	27.3	59	29.2	26	23.5	16.6
Be	1.28	3.08	1.12	3.65	3.4	1.57
Sc	12.3	10.2	16	7	7.61	2.63
V	73.5	59.1	144	20	26.9	3.38
Cr	3.63	18.4	41.3	5.61	5.2	12
Co	8.19	6.53	13.7	1.86	2.9	0.21
Ni	3.06	7.68	21	2.78	2.9	4.74
Cu	7.23	41.3	16	9.08	20.2	7.86
Zn	96.5	2084	80.5	164	308	59.5
Ga	21.3	16.5	17.7	20.9	21.6	19.6
Rb	99.8	251	47	166	232	351
Sr	564	160	497	163	183	72.4
Y	29.6	22.3	24.4	46.7	46.3	28.5
Mo	0.254	1.94	0.26	2.73	2.41	1.51
Cd	0.228	14.5	0.174	1.02	2	0.168
In	0.069	6.78	0.037	0.074	0.627	0.042
Sb	0.425	0.484	0.267	0.798	0.364	1.66
Cs	11.3	9.49	6.8	7.51	7.14	9.35
Ba	761	1129	482	623	729	514
La	40	28.8	32.5	86.4	91.7	36.1
Ce	84.5	56.7	67.4	178	187	76
Pr	10.9	7.05	8.64	22.1	23.3	9.17
Nd	44.1	27.9	35.7	86.4	90.9	32.2
Sm	8.23	5.33	6.89	15.8	16.6	6.42
Eu	1.69	1.22	1.63	1.76	1.95	0.283
Gd	6.57	4.18	5.13	11.2	12.2	5.09
Tb	1.13	0.695	0.911	2.01	1.99	0.951
Dy	5.6	4.36	4.92	9.84	9.72	4.33
Ho	1.04	0.785	0.849	1.57	1.8	0.901
Er	2.9	2.26	2.29	4.2	4.43	2.87
Tm	0.401	0.378	0.36	0.644	0.619	0.529
Yb	2.81	2.62	2.28	3.95	4.2	3.19
Lu	0.437	0.363	0.321	0.616	0.539	0.479
W	0.722	5.44	0.454	2.88	1.83	1.47
Re	<0.002	0.004	<0.002	0.005	0.006	0.004
Tl	1.04	3.88	0.325	2.11	3.47	4.92
Pb	13.5	32.9	9.79	134	17	77.8
Bi	0.088	2.4	0.225	0.28	0.925	0.088
Th	6.6	7.22	7.7	17.3	16.6	23.7
U	1.62	1.99	1.96	4.98	4.18	5.28
Nb	14	8.56	8.94	24.7	24.6	27.5
Ta	0.969	0.743	0.55	1.81	1.64	2.02
Zr	252	213	177	462	473	160
Hf	6.67	5.6	4.11	10.8	11.7	6.41

Ba anomaly. Geochronological and geochemical data indicate contrasting geochemical characteristics for the late Yanshanian and the Indosinian intrusions.

5.2. Mineral chemistry (EPMA)

Results of EMPA analyses of the phenocrysts including biotite, feldspar, hornblende, and quartz (TiO_2) from the intrusions are given in Table 3–6, respectively. A brief discussion of the results is given below.

5.2.1. Biotite

Biotite was analyzed in the monzonite-porphyry (sample 1321, three analyses), the syenite porphyry (five analyses, sample 1209), and in the dacite porphyry (sample 12, two analyses) (Table 3). The biotite can be classified as magnesio biotite in all three rock types, with one exception (ferro-biotite) (Fig. 8a). Biotite in the dacite porphyry appears to be of primary magmatic origin whereas biotite in both the monzonite porphyry and syenite porphyry has been re-equilibrated (Fig. 8b).

Table 2
Whole-rock major elements data of the representative intrusions from the Great Xing'an Range (data collected from Geng, 2006; location of the deposit shown on Fig. 1b).

Deposit	Rock types	SiO_2	TiO_2	Al_2O_3	Fe_2O_3	FeO	MnO	CaO	MgO	K_2O	Na_2O	P_2O_5	LOI	H_2O+
Cu polymetallic														
Dajing	Dacite porphyry	67.39	0.43	15.03	1.81	1.74	0.09	2.13	0.56	3.09	3.07	0.15	4.25	
Naoniushan	Plagioclase porphyry	79.18	0.03	13.09	0.31	0.63	0.03	1.04	0.60	0.66	3.40	0.30		
	Plagioclase porphyry	51.58	0.82	16.52	2.11	7.30	0.12	7.32	5.74	2.03	3.52	0.18	2.49	
	Plagioclase porphyry	53.28	0.97	14.68	1.52	7.78	0.10	9.98	5.92	0.50	3.71	0.24	1.71	
	Plagioclase porphyry	51.70	1.08	14.75	2.49	9.22	0.14	6.80	4.63	2.13	4.48	0.20	2.33	
	Plagioclase porphyry	48.18	1.08	17.11	2.79	9.58	0.12	8.19	5.26	3.23	1.78	0.17	2.04	
	Plagioclase porphyry	50.30	1.12	17.24	2.38	9.12	0.10	7.76	4.97	2.85	1.81	0.18	1.88	
	Granodiorite porphyry	68.96	0.47	15.95	0.45	1.12	0.01	2.05	1.16	5.45	4.18	0.01	0.62	
	Granodiorite porphyry	69.10	0.41	15.77	0.64	1.22	0.01	2.16	1.24	4.67	4.22	0.07	0.77	
Lianhuashan	Plagiogranite porphyry	69.94	0.33	14.85	0.68	0.87	0.03	1.81	0.79	3.50	4.54	0.10		
	Diorite porphyry	53.96	0.91	17.05	1.19	7.19	0.14	7.86	4.95	1.25	3.49	0.19	1.68	
	Diorite porphyry	54.94	0.95	16.87	1.15	7.04	0.15	4.11	3.69	2.05	4.40	0.24	4.23	
	Dacite porphyry	56.82	1.42	15.86	1.19	7.28	0.07	1.66	4.50	4.01	3.94	0.56	2.42	
	Dacite porphyry	56.76	1.42	14.96	1.65	7.45	0.07	1.51	4.86	4.02	3.71	0.56	2.57	
	Dacite porphyry	59.88	1.33	13.99	1.71	6.63	0.06	1.11	4.86	3.84	3.14	0.53	2.51	
	Granodiorite porphyry	67.97	0.38	15.86	0.85	2.18	0.04	2.02	1.24	1.44	6.35	0.13	1.42	
	Granodiorite porphyry	67.26	0.37	15.59	1.00	2.08	0.04	2.07	1.29	1.40	6.48	0.13	1.59	
	Granodiorite porphyry	61.24	0.69	15.69	1.31	4.89	0.08	3.86	3.06	2.19	4.11	0.16	2.12	
	Granodiorite porphyry	69.64	0.33	14.85	0.68	0.87	0.03	0.79	1.81	4.54	3.50	0.10		
	Granodiorite porphyry	69.41	0.34	15.73	0.79	1.50	0.06	1.90	1.05	3.04	4.60	0.10		
Budunhua	Granodiorite	64.18	0.45	15.48	0.97	3.80	0.07	3.72	1.54	2.78	4.22	0.13		
Ag polymetallic														
Jiawula	Plagioclase porphyry	67.03	0.77	14.40	3.03	1.68	0.13	2.08	1.50	2.46	5.08	0.19	2.49	2.01
	Quartz porphyry	80.40	0.15	11.25	0.59	0.61	0.04	0.70	0.92	3.57	0.06	0.02	2.34	1.92
	Syenite porphyry	67.51	0.62	15.16	0.35	2.03	0.08	1.39	0.70	5.90	3.41	0.13	2.38	1.75
	Plagioclase porphyry	73.01	0.41	13.05	1.50	1.23	0.08	0.97	1.10	3.85	3.41	0.06	2.28	1.74
Chagan	Granite porphyry	73.49	0.22	12.87	2.40	0.35	0.69	1.04	0.60	4.74	0.17	0.04	2.97	2.31
	Granite	71.42	0.21	15.18	1.86	0.82	0.04	0.81	0.70	5.02	3.62	0.09		0.24
	Granite	71.93	0.14	14.76	1.96	0.87	0.05	0.33	0.64	5.35	3.81	0.02		0.31
	Quartz porphyry	73.37	0.32	12.86	1.38	0.70	0.10	0.91	0.77	2.56	4.78	0.08	1.78	1.29

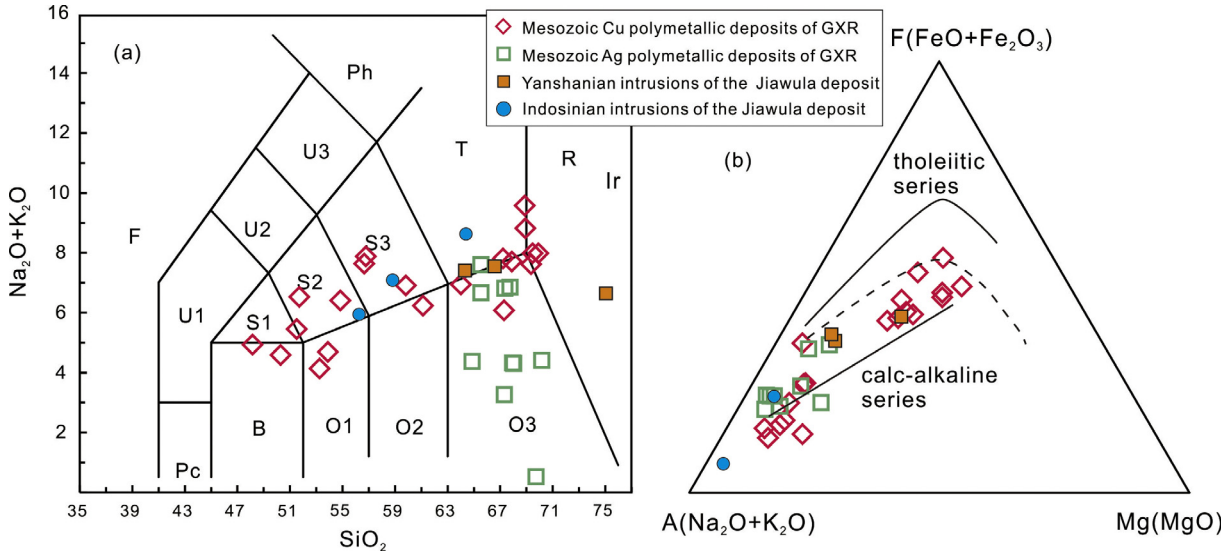

Fig. 4. TAS (a) and AFM (b) diagrams for the intrusions from the Mesozoic Cu and Ag polymetallic deposits of the Great Xing'an Rang (GXR) and the Jiawula deposit (data of the Great Xing'an Range from Geng, 2006). B: basalt; O1: basaltic andesite; O2: andesite; O3: dacite; R: rhyolite; T: trachyte or trachydacite; Ph: phonolite; S1: trachybasalt; S2: basaltic trachyandesite; S3: trachyandesite; Pc: picrobasalt; U1: basanite or tephrite; U2: phonotephrite; U3: tephriphonolite; F: foidite.

5.2.2. Feldspar

The EPMA results of feldspar in the intrusions of the Jiawula deposit are presented in Table 4 and Fig. 9a. Albite and oligoclase are the major feldspars in diorite porphyry. The albite content ranges between 67.0 and 73.7 mol% (sample 513), and between 89.7 and 98.6 mol% (sample 1302). In the monzonite porphyry, both orthoclase and plagioclase are present. Sanidine-feldspar in the syenite porphyry (sample 1209) shows an orthoclase content ranging from 48.9 to 94.6 mol%.

5.2.3. Hornblende

Euhedral hornblende phenocrysts in diorite porphyry (ten analyses) and monzonite porphyry (three analyses) can be classified as magnesio-hornblende (Leake et al., 1997) (Fig. 9b). They are characterized by a high MgO (average 46.6 wt% and 47.0 wt% respectively) and a relatively low FeO (average 15.3 wt% and 14.1 wt% respectively), CaO (average 11.6 wt% and 10.6 wt% respectively), and Al_2O_3 (averaged 6.7 wt% and 5.9 wt% respectively) concentrations. Na_2O, TiO_2, and MnO occur in minor amounts (Table 5).

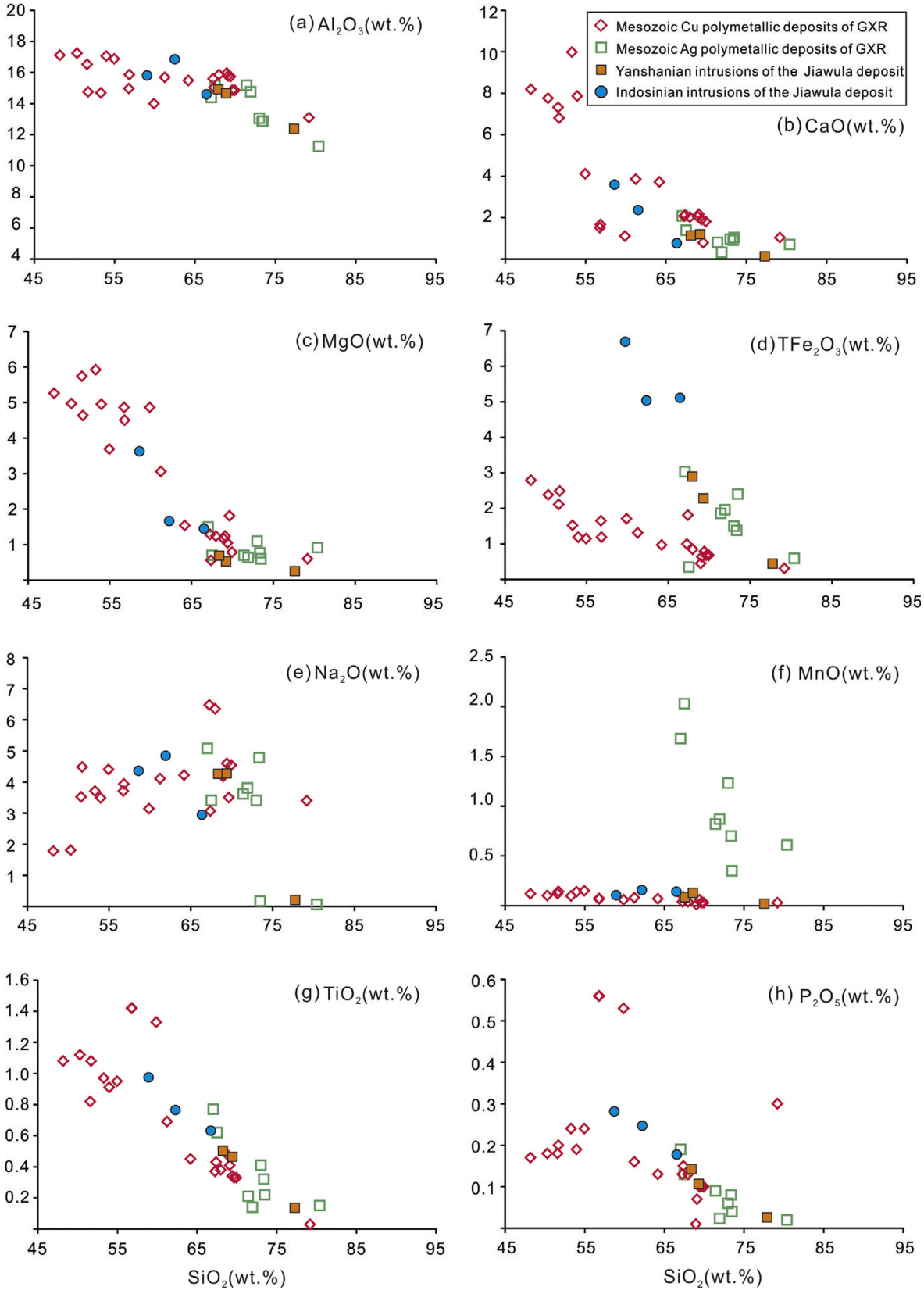

Fig. 5. Harker diagrams for the intrusions from the Mesozoic Cu and Ag polymetallic deposits of the Great Xing'an Rang and the Jiawula deposit (data of the Great Xing'an Range from Geng, 2006).

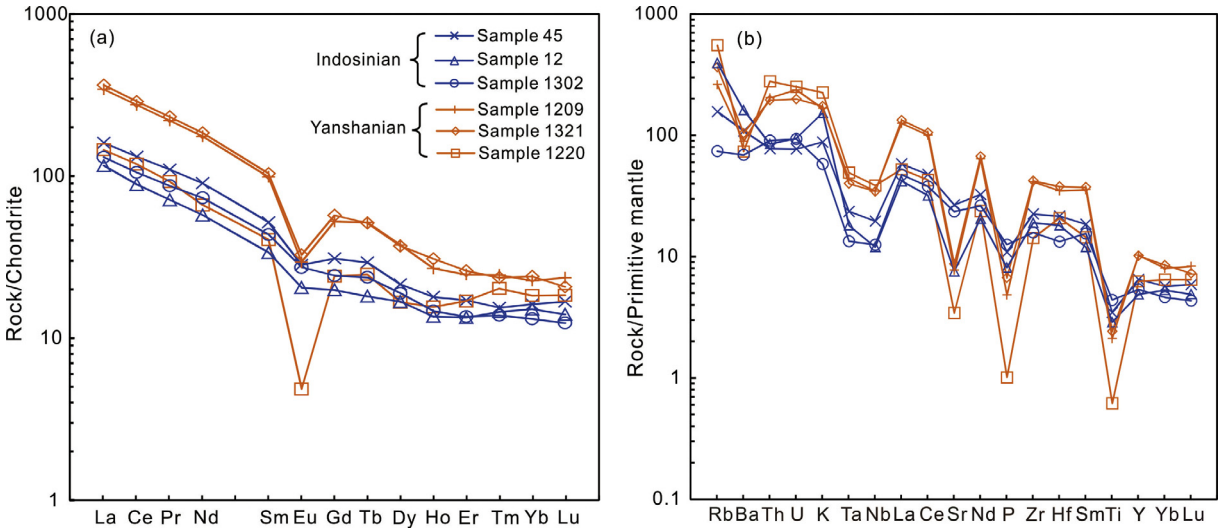

Fig. 6. Chondrite-normalized REE patterns and primitive-mantle-normalized trace element spider diagrams for the intrusions in the Jiawula deposit. Chondrite and primitive-mantle REE values are from Boynton (1984) and Sun and McDonough (1989), respectively.

Table 3
Representative EPMA results of biotite in wt%.

Sample No.	Mineral	SiO_2	TiO_2	Al_2O_3	Cr_2O_3	V_2O_3	$Fe_{total}O$	MgO	MnO	CaO	BaO	ZnO	Na_2O	K_2O	P_2O_5	Nb_2O_5	F	Cl	Total
1321	Biotite	31.20	1.43	15.73	0.00	0.10	23.35	13.48	0.67	0.00	0.02	0.13	0.02	3.50	0.00	0.00	0.51	0.02	90.17
1321	Biotite	32.77	1.19	15.65	0.01	0.12	22.00	12.52	0.54	0.01	0.03	0.12	0.00	4.27	0.00	0.03	0.56	0.03	89.87
1321	Biotite	32.04	1.84	15.37	0.03	0.18	22.40	12.44	0.51	0.25	0.03	0.15	0.03	4.18	0.00	0.05	0.81	0.01	90.33
1209	Biotite	36.04	3.26	13.12	0.07	0.10	19.01	11.69	0.47	0.00	0.25	0.09	0.37	8.68	0.03	0.00	1.74	0.08	95.05
1209	Biotite	37.32	2.91	12.53	0.03	0.00	19.61	11.70	0.45	0.00	0.09	0.24	0.25	9.06	0.00	0.04	1.95	0.05	96.25
1209	Biotite	34.88	3.00	13.26	0.05	0.11	23.97	8.19	0.53	0.00	0.58	0.34	0.32	8.36	0.00	0.02	0.84	0.09	94.63
1209	Biotite	37.97	2.29	12.27	0.01	0.06	18.52	12.46	0.40	0.00	0.06	0.00	0.18	9.17	0.01	0.05	2.14	0.07	95.70
1209	Biotite	35.50	2.35	13.17	0.19	0.11	22.27	9.76	0.58	0.00	0.12	0.11	0.10	8.24	0.00	0.04	0.89	0.07	93.59
12	Biotite	35.84	3.93	13.83	0.01	0.09	13.63	14.14	0.32	0.00	0.52	0.12	0.60	8.25	0.01	0.00	3.06	0.04	94.45
12	Biotite	35.94	4.09	13.67	0.00	0.03	13.39	14.11	0.17	0.00	0.59	0.10	0.66	8.46	0.00	0.00	3.05	0.04	94.33

5.2.4. Quartz

Quartz occurs mainly as idiomorphic or hypautomorphic phenocrysts in the quartz porphyry. The detection limit of titanium in quartz is 10 ppm for the special operating conditions as described in the analytical techniques section. The TiO_2 content in quartz phenocryst ranges from 0.008 to 0.030 wt% with a mean value of 0.016 wt%; the titanium content ranges from 48 to 180 ppm averaging at 96 ppm (Table 6).

5.3. Mineral geothermometry and oxygen fugacity

The TitanniQ (titanium-in-quartz) geothermometer is used to constrain the crystallization temperature of the quartz phenocryst. The presence of rutile implies that the activity of Ti can be set at unity (Fig. 3f). The temperature of quartz crystallization (or re-equilibration) can be calculated using the following equation (Wark and Watson, 2006):

$$T(^{\circ}C) = \frac{-3765}{\log(X_{Ti}^{qtz}) - 5.69} - 273 \quad (1)$$

where Ti concentrations in quartz (X_{Ti}^{qtz}) are in ppm. The calculated temperatures range between 666 and 823 °C with an average value of 734 °C (Table 6).

The two-feldspar thermometry has been developed by numerous researchers, such as Ghiorso (1984), Elkins and Grove (1990), Putirka (2008), and Benisek et al. (2010). In this study the two-feldspar thermometer of Putirka (2008) is considered to be the most appropriate for determining the crystallization temperature of feldspar in monzonite porphyry. The results, calculated using the Excel spreadsheet by Hora et al. (2013) and for pressures of 4–6 kbar, show two temperature ranges: 395–450 °C (average value of 429 °C) and 623–830 °C (average value of 738 °C).

Using the methods developed by Scaillet and Evans (1999) and Ridolfi et al. (2008, 2010), we used the compositions of hornblende in the diorite porphyry and monzonite porphyry to calculate the crystallization temperature and the oxygen fugacity. The calculated temperature of hornblende ranges between 852 and 894 °C (average value of 880 °C), and in monzonite porphyry from 844 to 888 °C (average value of 864 °C). The temperature data of the phenocrysts in the hypabyssal intrusions are summarized in Fig. 10a. The oxygen fugacity (expressed in $\log_{10}$ units relative to the NNO buffer) in the monzonite porphyry ranges from +1.02 to +1.55 (average value of +1.37), which is 0.3–0.4 $\log_{10}$ units higher than the oxygen fugacity in the diorite porphyry (+0.71 to +1.11, average value of +0.87) (Table 5; Fig. 10b).

5.4. Zircon U-Pb geochronology

Representative zircon cathode luminescence images with corresponding U-Pb ages for six samples from the Jiawula deposit are shown in Fig. 11. The results of zircon SHRIMP U-Pb dating are presented in Table 7 and Fig. 12. Based on age data presented in this study, the intrusive rocks can be classified into two groups. The first group represents the Indosinian granodiorite, dacite porphyry, and diorite porphyry, which were emplaced during the Late Permian to Early Triassic. The second group includes the quartz por-

Table 4
Representative EPMA results of feldspar in wt%.

Sample No.	SiO_2	TiO_2	Al_2O_3	Cr_2O_3	V_2O_3	Fe_TO	BaO	MgO	CaO	CuO	ZnO	MnO	NiO	SrO	Na_2O	K_2O	P_2O_5	Nb_2O_5	F	Cl	Total	Ab (mol%)	An (mol%)	Or (mol%)
Plagioclase																								
513	61.82	0.03	23.49	0.01	0.00	0.27	0.01	0.00	5.08	0.03	0.00	0.03	0.01	0.00	8.15	0.16	0.03	0.00	0.04	0.01	99.19	73.70	25.38	0.93
513	61.76	0.00	24.40	0.00	0.03	0.23	0.02	0.00	5.07	0.00	0.07	0.01	0.00	0.00	7.67	0.14	0.00	0.08	0.09	0.01	99.59	72.63	26.49	0.88
513	62.73	0.00	23.30	0.04	0.00	0.17	0.00	0.03	4.95	0.00	0.21	0.00	0.00	0.00	7.80	0.18	0.00	0.06	0.00	0.01	99.46	73.20	25.71	1.09
513	60.51	0.02	24.40	0.00	0.00	0.14	0.01	0.02	6.12	0.00	0.14	0.00	0.01	0.00	7.74	0.16	0.01	0.00	0.02	0.00	99.31	68.96	30.13	0.91
513	61.34	0.10	23.52	0.00	0.00	0.12	0.00	0.02	5.16	0.04	0.01	0.02	0.01	0.00	8.38	0.16	0.00	0.02	0.00	0.01	98.92	73.92	25.13	0.95
513	61.24	0.04	23.39	0.00	0.00	0.13	0.02	0.01	5.18	0.00	0.02	0.02	0.00	0.00	8.30	0.16	0.00	0.00	0.11	0.00	98.62	73.64	25.40	0.96
513	59.75	0.00	24.69	0.02	0.00	0.05	0.01	0.03	6.56	0.09	0.00	0.00	0.00	0.00	7.55	0.13	0.00	0.00	0.11	0.00	99.01	67.04	32.20	0.76
513	63.96	0.12	23.95	0.03	0.00	0.19	0.00	0.02	4.45	0.00	0.07	0.00	0.04	0.00	6.93	0.29	0.00	0.00	0.00	0.01	100.10	72.32	25.67	2.01
1302	69.83	0.04	20.47	0.01	0.05	0.10	0.00	0.03	0.22	0.04	0.00	0.00	0.04	0.00	5.12	0.15	0.03	0.01	0.00	0.05	96.20	95.88	2.24	1.89
1302	67.51	0.09	21.98	0.00	0.00	0.45	0.02	0.14	0.19	0.10	0.00	0.08	0.00	0.00	8.26	1.28	0.00	0.00	0.00	0.01	100.13	89.69	1.15	9.17
1302	69.62	0.02	20.79	0.01	0.00	0.05	0.05	0.00	0.29	0.03	0.00	0.00	0.02	0.00	7.15	0.11	0.00	0.02	0.06	0.01	98.23	96.86	2.18	0.95
1302	69.60	0.03	20.53	0.00	0.01	0.04	0.00	0.01	0.24	0.02	0.11	0.00	0.00	0.00	7.39	0.16	0.00	0.00	0.02	0.00	98.18	96.89	1.76	1.35
1302	67.29	0.03	20.55	0.00	0.00	0.04	0.05	0.00	0.19	0.00	0.04	0.00	0.01	0.00	10.69	0.07	0.00	0.00	0.00	0.00	98.96	98.60	0.98	0.42
1302	67.58	0.00	21.10	0.03	0.01	0.09	0.07	0.01	0.13	0.00	0.00	0.00	0.01	0.00	10.22	0.19	0.01	0.02	0.00	0.00	99.48	98.11	0.67	1.22
1302	67.29	0.01	22.10	0.02	0.03	0.18	0.03	0.07	0.30	0.00	0.01	0.00	0.00	0.00	8.62	0.42	0.00	0.01	0.04	0.01	99.14	95.15	1.81	3.04
1302	66.48	0.04	21.18	0.02	0.03	0.00	0.00	0.00	0.39	0.06	0.00	0.10	0.01	0.04	10.35	0.09	0.00	0.03	0.02	0.02	98.85	97.37	2.04	0.58
1302	67.05	0.00	20.71	0.00	0.03	0.01	0.00	0.01	0.34	0.02	0.03	0.03	0.02	0.12	10.53	0.07	0.00	0.00	0.00	0.04	99.05	97.81	1.75	0.45
1302	68.78	0.00	21.19	0.00	0.02	0.00	0.00	0.02	0.33	0.01	0.00	0.03	0.01	0.05	8.65	0.14	0.04	0.04	0.13	0.02	99.45	96.97	2.03	1.00
1321	67.26	0.02	21.85	0.00	0.00	0.07	0.04	0.02	0.39	0.01	0.00	0.01	0.02	0.00	9.59	0.33	0.00	0.00	0.04	0.00	99.66	95.65	2.15	2.19
1321	64.38	0.00	22.78	0.04	0.00	0.21	0.00	0.00	3.42	0.02	0.07	0.00	0.03	0.00	8.83	0.18	0.02	0.00	0.00	0.02	99.99	81.51	17.42	1.07
1321	59.40	0.00	25.01	0.00	0.00	0.34	0.02	0.00	7.06	0.00	0.04	0.00	0.01	0.00	7.24	0.30	0.00	0.03	0.10	0.02	99.60	63.88	34.39	1.73
1321	57.49	0.00	26.46	0.00	0.00	0.28	0.00	0.00	7.76	0.00	0.00	0.03	0.00	0.00	7.57	0.36	0.01	0.00	0.04	0.00	99.99	62.59	35.46	1.94
1209	65.70	0.09	20.55	0.00	0.00	0.98	0.00	0.17	2.01	0.00	0.00	0.00	0.03	0.00	6.33	0.47	0.00	0.01	2.71	0.01	99.06	81.69	14.30	4.01
Orthoclase																								
1321	64.90	0.00	18.48	0.03	0.05	0.07	0.03	0.00	0.00	0.03	0.00	0.03	0.00	0.00	0.32	15.72	0.00	0.05	0.22	0.01	99.93	2.99	0.00	97.01
1321	64.13	0.02	18.76	0.00	0.01	0.05	0.10	0.00	0.00	0.00	0.00	0.00	0.01	0.00	1.22	14.58	0.01	0.00	0.00	0.01	98.90	11.25	0.02	88.73
1321	65.26	0.00	18.26	0.01	0.00	0.00	0.09	0.00	0.00	0.00	0.00	0.00	0.00	0.00	0.28	15.20	0.00	0.01	0.00	0.03	99.12	2.75	0.00	97.25
1321	66.81	0.00	19.17	0.00	0.00	0.17	0.00	0.00	0.14	0.05	0.08	0.00	0.00	0.00	4.68	9.16	0.02	0.00	0.11	0.01	100.38	43.42	0.73	55.86
1321	67.28	0.04	19.19	0.01	0.00	0.14	0.01	0.00	0.15	0.00	0.00	0.04	0.01	0.00	4.79	8.63	0.00	0.03	0.00	0.04	100.38	45.41	0.76	53.82
1209	66.22	0.04	19.13	0.02	0.00	0.16	0.06	0.00	0.25	0.00	0.04	0.00	0.00	0.00	2.75	10.70	0.00	0.02	0.00	0.02	99.42	27.67	1.40	70.93
1209	65.96	0.01	18.69	0.02	0.00	0.17	0.00	0.00	0.14	0.00	0.08	0.00	0.00	0.00	5.44	8.03	0.00	0.02	0.00	0.03	98.61	50.37	0.71	48.92
1209	65.75	0.00	18.65	0.00	0.00	0.08	0.03	0.00	0.01	0.00	0.00	0.01	0.00	0.00	0.53	14.37	0.02	0.06	0.12	0.01	99.64	5.33	0.04	94.63
1209	64.81	0.00	18.46	0.00	0.03	0.19	0.02	0.00	0.00	0.02	0.00	0.00	0.00	0.00	0.34	15.27	0.00	0.06	0.00	0.06	99.26	3.27	0.00	96.73

Table 5
Representative EPMA results of hornblende in wt% and calculation results of temperature and oxygen fugacity (expressed as $\log_{10}$ units relative to the NNO buffer).

No.	SiO_2	TiO_2	Al_2O_3	$Fe_{total}O$	CaO	MgO	Na_2O	K_2O	MnO	F	Cl	Fe^{2+}	Mg	Ca	Na	K	Si*	T(°C)	Mg*	ΔNNO
513-1	46.26	0.60	7.15	16.57	11.43	11.63	1.15	0.55	1.01	0.35	0.04	1.54	2.62	1.85	0.34	0.11	7.57	894	2.89	0.74
513-2	46.27	0.69	6.95	16.15	11.60	11.56	1.16	0.46	0.83	0.56	0.05	1.42	2.61	1.88	0.34	0.09	7.62	887	2.88	0.72
513-3	46.73	0.62	6.87	15.98	11.67	11.93	1.06	0.43	0.72	0.19	0.02	1.43	2.68	1.89	0.31	0.08	7.62	887	2.94	0.83
513-4	46.73	0.51	6.63	15.38	11.65	12.03	0.90	0.44	0.80	0.16	0.03	1.33	2.73	1.90	0.26	0.09	7.70	875	3.01	0.94
513-5	45.89	0.39	7.08	16.23	11.46	11.66	1.18	0.44	0.86	0.49	0.05	1.49	2.65	1.87	0.35	0.09	7.61	889	2.94	0.82
513-6	45.78	0.85	6.88	15.42	11.36	11.56	1.26	0.73	0.88	0.46	0.05	1.40	2.63	1.86	0.37	0.14	7.62	886	2.87	0.71
513-7	45.63	0.43	7.29	15.93	11.55	11.57	1.15	0.48	0.87	0.66	0.04	1.43	2.63	1.89	0.34	0.09	7.60	889	2.93	0.80
513-8	46.84	0.57	5.63	14.57	11.58	12.23	0.80	0.37	0.82	0.53	0.03	1.13	2.80	1.90	0.24	0.07	7.85	852	3.11	1.09
513-9	48.72	0.48	6.11	14.78	12.06	12.77	0.75	0.37	0.79	0.11	0.01	1.14	2.82	1.92	0.22	0.07	7.80	859	3.12	1.11
513-10	46.75	0.69	6.66	16.11	11.83	12.06	0.92	0.43	0.75	0.40	0.03	1.40	2.71	1.91	0.27	0.08	7.65	882	2.99	0.90
Mean	46.56	0.58	6.73	15.71	11.62	11.90	1.03	0.47	0.83	0.39	0.03	1.37	2.69	1.89	0.30	0.09	7.66	880	2.97	0.87
Min	45.63	0.39	5.63	14.57	11.36	11.56	0.75	0.37	0.72	0.11	0.01	1.13	2.61	1.85	0.22	0.07	7.57	852	2.87	0.71
Max	48.72	0.85	7.29	16.57	12.06	12.77	1.26	0.73	1.01	0.66	0.05	1.54	2.82	1.92	0.37	0.14	7.85	894	3.12	1.11
1321-1	45.40	0.88	6.65	15.27	10.71	12.77	2.34	0.95	0.99	1.71	0.05	1.45	2.85	1.72	0.68	0.18	7.61	888	3.06	1.02
1321-2	47.96	0.58	5.61	13.40	10.61	14.30	2.17	0.79	1.08	1.37	0.05	1.10	3.14	1.67	0.62	0.15	7.90	844	3.38	1.55
1321-3	47.76	0.85	5.50	13.23	10.58	14.44	2.18	0.49	0.92	1.56	0.05	1.01	3.17	1.67	0.62	0.09	7.80	860	3.38	1.54
Mean	47.04	0.77	5.92	13.97	10.63	13.83	2.23	0.74	1.00	1.55	0.05	1.19	3.05	1.69	0.64	0.14	7.77	864	3.27	1.37
Min	45.40	0.58	5.50	13.23	10.58	12.77	2.17	0.49	0.92	1.37	0.05	1.01	2.85	1.67	0.62	0.09	7.61	844	3.06	1.02
Max	47.96	0.88	6.65	15.27	10.71	14.44	2.34	0.95	1.08	1.71	0.05	1.45	3.17	1.72	0.68	0.18	7.90	888	3.38	1.55

The detailed calculation method of T(°C) and ΔNNO is based on Ridolfi et al. (2010).

Table 6
Representative EPMA results in wt% and temperature calculations results based on the Ti-in-quartz geothermometer.

Sample No.	SiO_2	Na_2O	MgO	Al_2O_3	K_2O	CaO	FeO	Cr_2O_3	TiO_2	Total	Ti (10^{-6})	T (°C)
1220	99.26	0.01	0.01	0.02	0.00	0.01	0.00	0.00	0.012	99.32	72	709
1220	99.38	0.00	0.03	0.02	0.01	0.00	0.00	0.00	0.014	99.46	84	727
1220	99.50	0.10	0.01	0.02	0.02	0.02	0.00	0.01	0.026	99.71	156	804
1220	99.16	0.00	0.02	0.02	0.00	0.01	0.01	0.00	0.013	99.23	78	718
1220	99.70	0.00	0.01	0.02	0.00	0.00	0.00	0.02	0.014	99.76	84	727
1220	99.11	0.00	0.01	0.01	0.01	0.00	0.00	0.00	0.011	99.15	66	700
1220	99.08	0.02	0.03	0.01	0.01	0.02	0.02	0.01	0.008	99.20	48	666
1220	99.64	0.06	0.11	0.05	0.04	0.04	0.00	0.02	0.030	99.98	180	823
Min	99.08	0.00	0.01	0.01	0.00	0.00	0.00	0.00	0.008	99.20	48	666
Max	99.70	0.10	0.11	0.05	0.04	0.04	0.02	0.02	0.030	99.76	180	823
Average	99.35	0.02	0.03	0.02	0.01	0.01	0.01	0.01	0.016	99.52	96	734

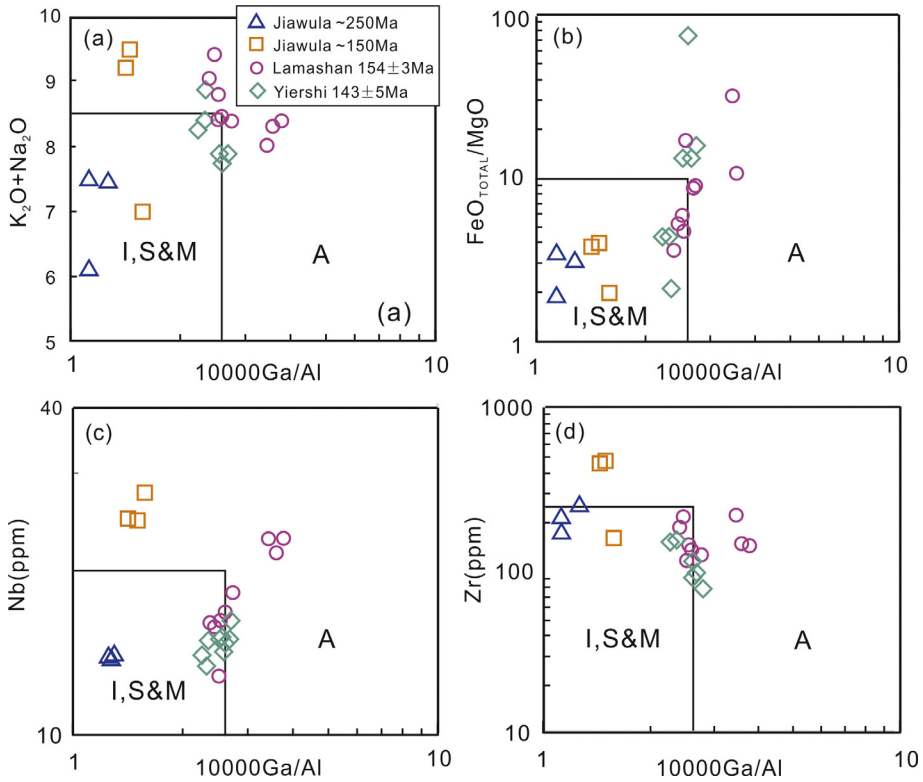

Fig. 7. Ga/Al versus $K_2O + Na_2O$ (a), FeO_T/MgO (b), Nb (c) and Zr (d) classification diagrams of the Jiawula, Lamashan and Yuershi granitoids in the Great Xing'an Range (after Whalen et al., 1987; Rb-Sr isochron ages and geochemical data of Lamashan and Yuershi from Wu et al., 2003b).

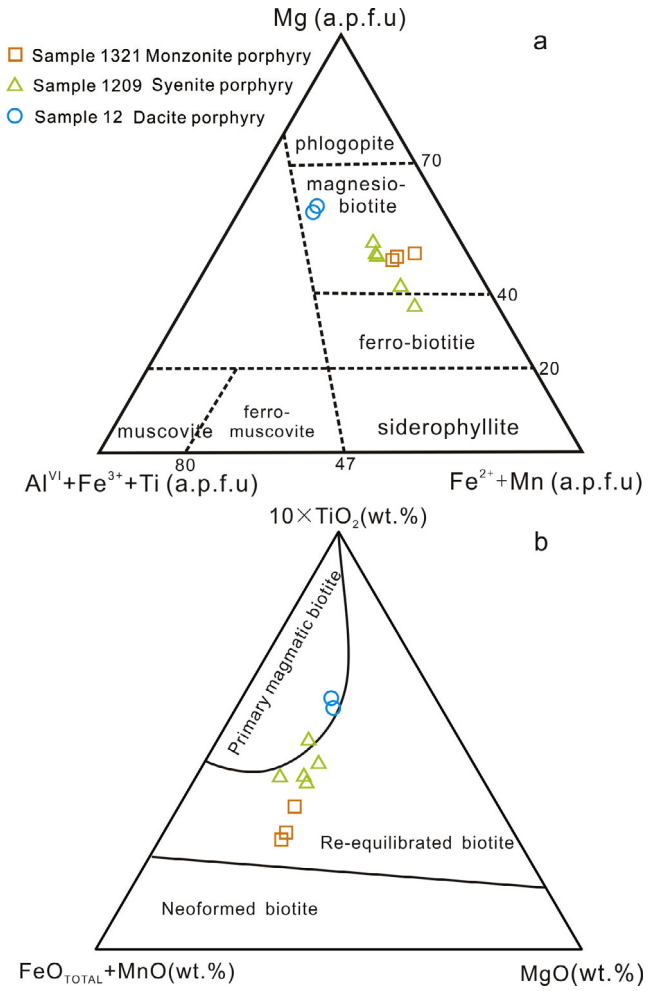

Fig. 8. Compositional plots of biotite from the intrusions in the Jiawula deposit. (a) Biotite classification ternary diagram (Foster, 1961; Zhang et al., 2015b); (b) Domains of the primary magmatic, re-equilibrated and neoformed biotites (Nachit et al., 2005); a.p.f.u. = atoms per formula unit.

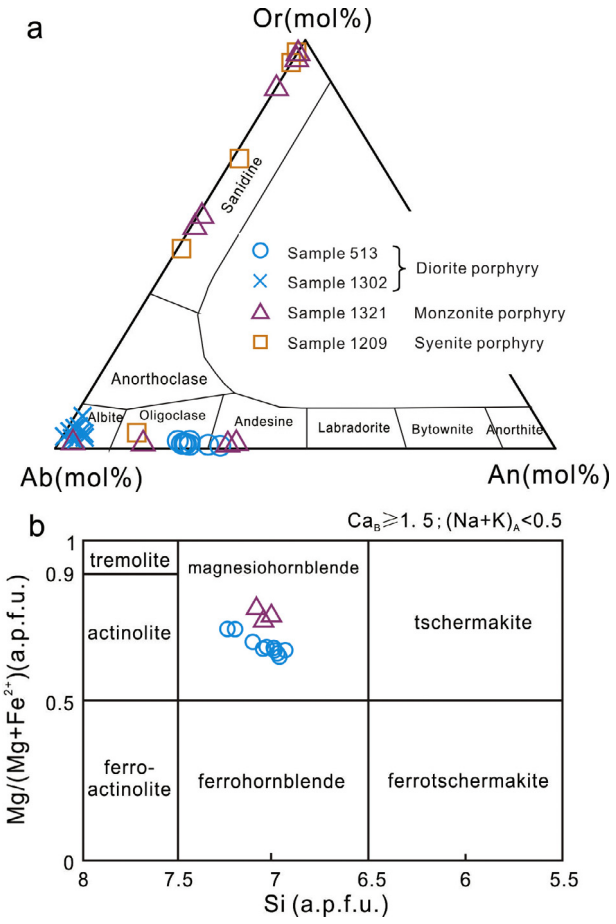

Fig. 9. Classification of (a) feldspar phenocrysts (after Deer et al., 1992) and (b) amphibole phenocrysts (after Leake et al., 1997) in the Jiawula deposit intrusives. a.p.f.u. = atoms per formula unit.

phyry, syenite porphyry, and monzonite porphyry, which are part of the late Yanshanian intrusive event in the Late Jurassic.

5.4.1. Late Permian to Early Triassic

5.4.1.1. Granodiorite. Most of the twelve zircon grains in sample 45 are elongated prisms, showing sizes of 40–60 × 100–300 μm with aspect ratios of about 2.5:1–5:1. Prismatic faces and oscillatory zoning are common, indicating a magmatic source. The U and Th contents range from 285 to 839 ppm, and 162 to 452 ppm, respectively (Th/U mass ratio of 0.37–0.59). The $^{206}Pb/^{238}U$ age for the granodiorite was determined to be 254 ± 2.0 Ma (n = 12, MSWD = 1.2) (Fig. 12a).

5.4.1.2. Dacite porphyry. Zircons in sample 12 (50–100 × 80–120 μm) are euhedral, short prismatic, and most of them show oscillatory zoning. Among the eight analyzed spots, seven spots yield a weighted mean $^{206}Pb/^{238}U$ age of 252.9 ± 4.8 Ma (MSWD = 2.4). The U contents of the seven spots range between 184 and 1443 ppm. The Th contents show a range of 159–1649 ppm, with Th/U mass ratios of 0.48–1.70. One spot analysis was excluded because of the high U content (2264 ppm) (Fig. 12b).

5.4.1.3. Diorite porphyry. The zircon grains in sample 1302 are mostly euhedral prismatic and show oscillatory zoning. Their grain size ranges from 50–150 × 50–100 μm with aspect ratios of about 1:1–4:1. Their U content shows a range of 105 to1750 ppm and Th content ranges between 74 and 615 ppm (Th/U mass ratios range from 0.83 to 0.21).The age data from this sample can be divided into two groups: 457.8 ± 7.1 Ma (n = 3, MSWD = 0.64) and 247.8 ± 4.1 Ma (n = 2, MSWD = 0.66) (Fig. 12c).

5.4.2. Late Jurassic

5.4.2.1. Quartz porphyry. The zircon grains of sample 1220 show a size range of 70–140 × 50–110 μm and aspect ratios of about 1.5:1–3:1. The grains are euhedral, prismatic and show weak oscillatory zoning with medium brightness. Eleven analyses show U contents of 107–772 ppm, Th contents of 154–718 ppm, and Th/U mass ratios ranging between 0.62 and 1.49. The age data are concordant, yielding a $^{206}Pb/^{238}U$ age of 150.1 ± 1.8 Ma (n = 11, MSWD = 1.4) (Fig. 12d).

5.4.2.2. Syenite porphyry. In sample 1209, the zircon grains range from in size 80–140 × 70–100 μm with aspect ratios of about 1.2:1–2:1. They are all euhedral and some are oscillatory zoned. A total of 11 spots were analyzed. The U and Th contents vary between 37 and 396 ppm, and between 52 and 505 ppm, respectively (Th/U mass ratios of 0.76–1.60). The $^{206}Pb/^{238}U$ ages range from 144.8 to 159.9 Ma (Fig. 12e), with the weighted mean age of 148.8 ± 2.2 Ma (MSWD = 1.5).

5.4.2.3. Monzonite porphyry. Zircons in sample 1321 range in size from 40–80 × 70–110 μm with aspect ratio 2:1–1.2:1. The grains are zoned and stubby prismatic with U contents of 42–317 ppm,

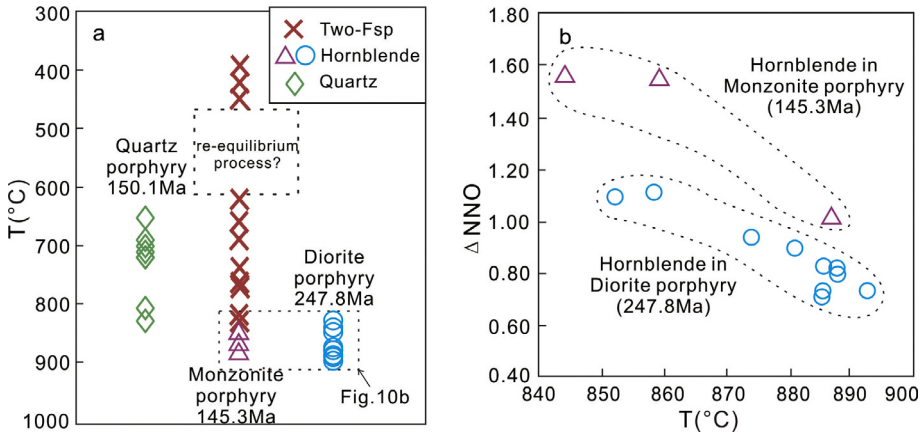

Fig. 10. Plots of (a) summary of phenocryst geothermometry and (b) temperature versus relative oxygen fugacity (expressed relative to the NNO buffer) of the intrusions in the Jiawula deposit.

Th of 52–430 ppm, and Th/U mass ratios of 0.80–1.66. Among the total of 12 spot analyses, 11 yielded a weighted mean $^{206}Pb/^{238}U$ age of 145.3 ± 1.9 Ma (MSWD = 1.6) (Fig. 12f). One spot was excluded because of the low U and Th content (13 and 11 ppm, respectively).

5.5. Sr-Nd isotopes

Whole-rock Rb-Sr and Sm-Nd isotope compositions of representative samples including syenite porphyry, monzonite porphyry, quartz porphyry, and diorite porphyry are listed in Table 8. All of the samples have negative $\varepsilon_{Nd}(t)$ ranging from −3.4 to −0.2 and initial $^{87}Sr/^{86}Sr$ values vary between 0.70458 and 0.70522. The Nd model age (T_{DM}) is 1064 Ma for quartz porphyry (sample 1220), 988 Ma (sample 1209) for syenite porphyry, 1011 Ma (sample 1321) for monzonite porphyry, and 1021 Ma for diorite porphyry (sample 1302). The T_{2DM} ages range from 1038 to 1216 Ma among all the analyzed samples. The crustal residence age and the history of crustal formation can be inferred from these data, which will be discussed in the next section.

6. Discussion

6.1. Timing of magmatism

Previous study shows an age of 139.2 ± 0.5 Ma for the quartz-monzonite-porphyry based on a single-grain zircon U-Pb LA-ICP-MS method (Qin et al., 1996). Qin et al. (1998) obtained two Rb-Sr isochron ages of monzonitic granite and granodiorite (ca. 225 Ma and ca. 211 Ma, respectively), suggesting the presence of Indosinian granitoids. However, the complete framework of the magmatism sequence in Jiawula has not been established.

Here, six samples of the intrusions including granodiorite, dacite porphyry, diorite porphyry, quartz porphyry, syenite porphyry, and monzonite porphyry were dated in this study in order to tightly constrain the timing and the relationship with mineralization. The quartz porphyry and syenite porphyry show ages of 150.1 ± 1.8 Ma and 148.8 ± 2.2, respectively, whereas the monzonite porphyry was emplaced at 145.3 ± 1.9 Ma. The mineralization age of the Jiawula deposit has been, as mentioned previously, reported to be 142.7 ± 1.3 Ma by Li et al. (2014b). The 145.3 ± 1.9 Ma age of monzonite porphyry confirms mineralization following the major magmatic phase.

Another magmatic event occurred in the Late Permian to Early Triassic represented by the granodiorite formation at 254 ± 2 Ma and the dacite porphyry at 252.9 ± 4.8 Ma. The diorite porphyry (sample 1302) shows two age groups: 457.8 Ma and 247.8 Ma. Field relationships show that the diorite porphyry intruded into the granodiorite and was cut by the ore bodies, indicating that the diorite porphyry is later than the granodiorite and earlier than the mineralization (Fig. 3k and l). The age of 247.8 ± 4.1 Ma, therefore, represents the emplacement age of diorite porphyry, and the age of 457.8 ± 7.1 Ma probably represent inherited xenocrystic zircons.

Previous studies have documented major magmatic and mineralization events in NE China (Ouyang et al., 2013; Liu et al., 2014; Zhou et al., 2015; Wang et al., 2015) during the Triassic (240–205 Ma), Early-Middle Jurassic (190–165 Ma), Late Jurassic (155–145 Ma), and Early Cretaceous (140–100 Ma). Late Permian to Early Triassic magmatism in the Great Xing'an Range, on the other hand, has rarely been reported so far (Tang et al., 2016). Therefore, the ca. 254–247 Ma magmatism in Jiawula is essential to understand magmatism during this time period.

In summary, the first magmatic event in Jiawula occurred from about 254 Ma–247 Ma and is exemplified by the emplacement of granodiorite, dacite porphyry, and diorite porphyry. The second event at 150 Ma–145 Ma started with the emplacement of quartz porphyry followed by syenite porphyry and monzonite porphyry.

6.2. Genetic classification of granitoid intrusions

Investigations of the Late Jurassic to Early Cretaceous granites in the Great Xing'an Range area have shown that many of them are A-type granite. For example, fine-grained granite (zircon U-Pb age 145.2 ± 0.5 Ma) in Taolaituo, K-feldspar granite and granite porphyry in the Huanggang (zircon U-Pb age 136.7 ± 1.1 Ma and 136.8 ± 0.57 Ma, respectively) were classified as A-type granites (Jahn et al., 2001; Wu et al., 2002; Zhou et al., 2012, 2015). However, recent studies also found that I-type granitoids are present in the Great Xing'an Range, including the Aobaotu (zircon U-Pb age of 139.1 ± 0.5 Ma), Yiershi (zircon U-Pb age of 137 ± 2 Ma; Rb-Sr isochron age of 143 ± 5 Ma) and Lamashan (whole-rock Rb-Sr isochron age of 154 ± 3 Ma) plutons (Wu et al., 2003a,b; Zhou et al., 2015).

Strontium and neodymium isotopic data can be very useful to discriminate I-type from S-type and M-type granitoid. Evidence of crust-mantle interaction is demonstrated by Sr-Nd isotope systematics (Fig. 13). Besides, S-type granitiods have relatively high initial $^{87}Sr/^{86}Sr$ values (>0.70900) and low ε_{Nd} value (−6 to −10) compared to I-type granitoids (King et al., 1997). Therefore, intrusions of both Indosinian and Yanshanian in Jiawula are considered not to be S- or M-type granitoids.

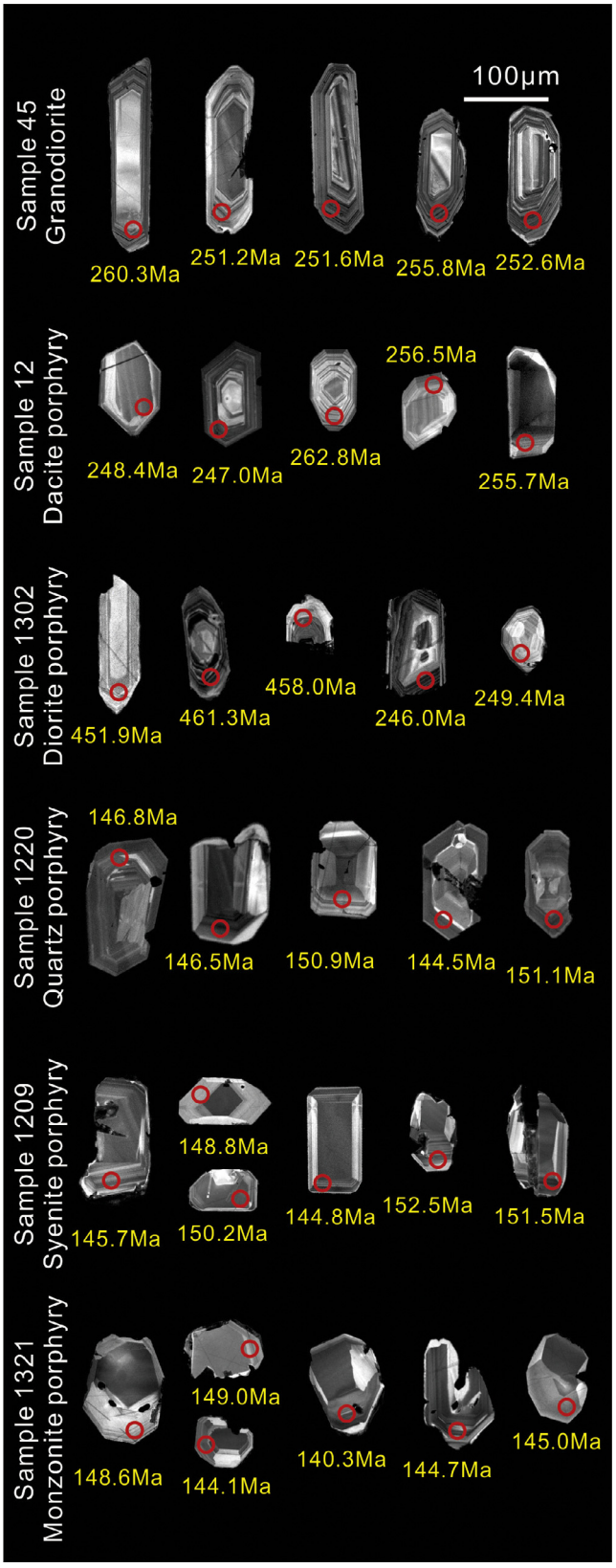

Fig. 11. Cathodoluminescence images of zircons with laser spots and ages in Ma. (a) to (c): Late Permian to Early Triassic (Indosinian); (d) to (f): Late Jurassic (Yanshanian) intrusions.

The intrusions in Jiawula show a depletion of HFSEs (e.g. Ta, Nb, P, and Ti) and are enriched in LILEs (e.g. Rb), similar to I-type granitoids (Fig. 6b) (King et al., 1997; Wu et al., 2002). Furthermore, the low contents of Ga, Zr, Nb, and Zn indicate that the Jiawula intrusions represent fractionated I-type granitoids. This is confirmed by the fact that the Indosinian and some of the Yanshanian intrusions in Jiawula show typical geochemical characteristics of I-type granites (Fig. 7) (Whalen et al., 1987).

One issue that cannot be ignored is the fact that Late Jurassic Intrusions in Jiawula show transitional geochemical features (Fig. 7a, c, d), similar to the Late Jurassic Lamashan and Yuershi plutons in the Great Xing'an Range (location shown on Fig. 1b) (Wu et al., 2003a,b). Even though they are all considered to be I-type granites, the geochemical differences of the Late Jurassic intrusions in Jiawula are apparent. They are characterized by a much lower Ga/Al mass ratio which resulted from a higher content of aluminum in comparison to the Lamashan and Yuershi intrusions. The higher content of aluminum in the intrusions in Jiawula compared to those in Lamashan and Yuershi might indicate more involvement of continental crustal component. High Ga/Al mass ratios appear to be typical of A-type granites (Whalen et al., 1987). Late Jurassic intrusions in Jiawula cannot be considered to be A-type because of the low Ga/Al values and they should rather be classified as a fractionated I-type.

6.3. Geodynamics and origin of the magma

It has been proposed that the Erguna block collided with the Xing'an block during the Early Paleozoic (Zhang and Tang, 1989; Ge et al., 2005; Zheng et al., 2013). The final closure of the Paleo-Asian Ocean is thought to have occurred during the Late Permian to the Early Triassic at ~250 Ma along the Xar Moron-Changchun suture progressively from west to east (Xiao et al., 2003; Xu et al., 2009; Wu et al., 2011). However, it is believed that the Early Mesozoic igneous rocks were not closely related to the Paleo-Asian tectonic regime but rather to the Mongol-Okhotsk plate tectonic environment (Tang et al., 2014, 2016). The subduction of the Mongol-Okhotsk oceanic plate towards the south beneath the Erguna massif is the main plate tectonic event during the early Mesozoic (Tang et al., 2016). The I-type characteristics of the ca. 254–247 Ma intrusions in Jiawula suggest an active continental margin setting related to the southward subduction of the Mongol-Okhotsk oceanic plate.

During the Mesozoic, the Xing'an Mongolia Orogenic Belt was affected by the widespread emplacement of Late Mesozoic volcanic and granitic rocks (Lin et al., 2004; Ge et al., 2005; Zhang et al., 2011; Wu et al., 2011). The Mongol-Okhotsk Ocean closure in the Middle Jurassic exerted some influence on the Great Xing'an Range area (Kravchinsky et al., 2002; Tomurtogoo et al., 2005). The subduction direction of the Paleo-Pacific plate changed to the north or northwest at ~140 Ma (Maruyama et al., 1997; Mao et al., 2005), causing large-scale delamination of the thickened continental crust and upwelling of the asthenosphere (Wang et al., 2006). The enrichment of U, Th, and K in ca. 154–147 Ma intrusions of Jiawula can be recognized as the evidence of the thickened continental crust before delamination (Sylvester, 1998; Zhu et al., 2009). The ~150 Ma magmatic episode in Jiawula happened after the closure of the Mongol-Okhotsk Ocean and before large-scale delamination of the thickened continental crust. This suggests the post-orogenic extensional geochemical A-type characteristics and the possible partial melting of the lower crust substance exemplified by typical I-type geochemical features.

The granitoids have negative $\varepsilon_{Nd}(t)$ values of −3.4 to −1.5, implying that the Jiawula Jurassic granitoids incorporated a relatively older crust component in contrast to the other intrusions in the Great Xing'an Range area which show positive $\varepsilon_{Nd}(t)$ values (Fig. 13). In addition, the majority of samples in both Xing'an and Songliao blocks show model ages younger than 1000 Ma and many of them even younger than 800 Ma (Wu et al., 2003b). Jurassic

Table 7
SHRIMP Th-U-Pb zircon data for samples from the intrusions of the Jiawula deposit, NE China.

Spot	$^{206}Pb_c$ %	U ppm	Th ppm	$^{232}Th/^{238}U$	$^{206}Pb*$ ppm	$^{206}Pb/^{238}U$ Age		$^{208}Pb/^{232}Th$ Age		Total $^{238}U/^{206}Pb$	±%	Total $^{207}Pb/^{206}Pb$	±%	$^{238}U/^{206}Pb^*$	±%	$^{207}Pb^*/^{206}Pb^*$	±%	$^{207}Pb^*/^{235}U$	±%	$^{206}Pb^*/^{238}U$	±%	err corr
JWL45																						
45-1	0.54	508	183	0.37	18.1	260.3	±3.3	240	±15	24.14	1.3	0.0515	2.6	24.27	1.3	0.0471	5.8	0.268	6.0	0.04120	1.3	.219
45-2	0.88	436	175	0.41	15.2	255.1	±4.1	200	±16	24.56	1.6	0.0554	2.7	24.78	1.6	0.0483	6.4	0.269	6.6	0.04036	1.6	.245
45-3	0.13	554	284	0.53	18.9	251.2	±3.8	239.1	±6.5	25.14	1.5	0.0535	2.5	25.17	1.5	0.0525	2.7	0.2875	3.1	0.03973	1.5	.493
45-4	–	474	186	0.41	16.4	255.8	±3.2	273.6	±7.8	24.83	1.3	0.0525	2.7	24.71	1.3	0.0567	2.5	0.3162	2.8	0.04048	1.3	.456
45-5	0.78	415	176	0.44	14.2	249.4	±3.3	221	±14	25.16	1.3	0.0550	2.7	25.36	1.3	0.0488	6.2	0.265	6.3	0.03944	1.3	.214
45-6	0.19	839	452	0.56	29.5	258.3	±3.0	246.9	±5.1	24.41	1.2	0.0540	1.9	24.46	1.2	0.0525	2.1	0.2960	2.4	0.04088	1.2	.495
45-7	0.49	554	241	0.45	19.1	252.6	±3.2	242	±14	24.90	1.3	0.0524	2.4	25.03	1.3	0.0485	6.2	0.267	6.3	0.03996	1.3	.206
45-8	0.93	410	164	0.41	14.0	248.8	±4.0	227	±17	25.18	1.6	0.0568	2.8	25.42	1.6	0.0494	7.0	0.268	7.2	0.03935	1.6	.228
45-9	0.38	316	163	0.53	11.0	255.1	±3.6	263	±13	24.68	1.4	0.0592	3.1	24.77	1.4	0.0562	5.9	0.313	6.0	0.04037	1.4	.238
45-10	0.78	436	229	0.54	15.0	251.6	±3.4	224	±16	24.92	1.3	0.0520	2.8	25.12	1.4	0.0457	9.1	0.251	9.2	0.03981	1.4	.152
45-11	0.42	591	261	0.46	20.2	250.7	±3.1	238.1	±9.8	25.11	1.3	0.0571	2.3	25.21	1.3	0.0537	4.0	0.294	4.2	0.03966	1.3	.302
45-12	0.57	285	162	0.59	10.1	258.7	±3.9	235	±19	24.28	1.4	0.0564	3.3	24.42	1.5	0.0519	9.9	0.293	10	0.04095	1.5	.154
JWL12																						
12-1	1.56	312	237	0.78	10.7	248.4	±3.6	216	±13	25.06	1.4	0.0562	3.2	25.46	1.5	0.0436	11	0.236	11	0.03928	1.5	.138
12-2	1.32	404	295	0.75	14.1	252.5	±3.5	215	±11	24.70	1.3	0.0582	2.8	25.03	1.4	0.0475	7.6	0.262	7.8	0.03994	1.4	.179
12-3	0.53	1004	1649	1.70	34.4	250.6	±2.9	233.4	±3.7	25.09	1.2	0.05381	1.8	25.22	1.2	0.0496	2.7	0.2711	2.9	0.03964	1.2	.406
12-4	0.33	1443	1478	1.06	50.5	256.5	±2.9	238.1	±3.5	24.55	1.1	0.05233	1.5	24.63	1.1	0.04972	1.6	0.2783	2.0	0.04059	1.1	.580
12-5	0.58	644	299	0.48	21.7	247.0	±3.1	235	±10	25.45	1.2	0.0550	2.3	25.60	1.3	0.0504	4.7	0.271	4.8	0.03906	1.3	.261
12-6	0.73	265	173	0.67	9.54	262.8	±3.9	248	±16	23.86	1.4	0.0571	3.6	24.03	1.5	0.0513	9.5	0.294	9.6	0.04161	1.5	.156
12-7	0.28	2264	680	0.31	83.1	269.1	±3.0	231.6	±6.7	23.39	1.1	0.05252	1.1	23.46	1.1	0.05031	1.9	0.2957	2.2	0.04263	1.1	.515
12-8	1.62	184	159	0.89	6.50	255.7	±4.0	255	±14	24.31	1.5	0.0678	3.6	24.71	1.6	0.0548	9.0	0.306	9.1	0.04047	1.6	.176
JWL1302																						
1302-1	0.27	680	274	0.42	22.8	246.0	±3.1	234	±14	25.64	1.2	0.0538	2.6	25.71	1.3	0.0516	5.8	0.277	5.9	0.03889	1.3	.214
1302-2	0.24	1750	352	0.21	59.4	249.4	±2.9	220.4	±7.5	25.29	1.2	0.05116	1.6	25.35	1.2	0.04927	1.8	0.2680	2.2	0.03945	1.2	.541
1302-3	0.55	240	155	0.67	15.0	451.9	±6.6	418	±22	13.70	1.4	0.0602	2.5	13.77	1.5	0.0557	6.7	0.558	6.9	0.0726	1.5	.219
1302-5	0.38	315	157	0.51	20.0	458.0	±8.2	415	±23	13.53	1.8	0.0579	2.4	13.58	1.9	0.0548	5.6	0.557	5.9	0.0736	1.9	.316
1302-7	0.13	1379	615	0.46	88.0	461.3	±5.1	456.8	±8.5	13.46	1.1	0.05697	1.1	13.48	1.1	0.05588	1.5	0.571	1.9	0.07417	1.1	.597
JWL1209																						
1209-1	1.95	396	505	1.32	7.93	145.7	±3.3	138	±10	42.90	1.9	0.0646	5.4	43.7	2.3	0.049	23	0.155	23	0.02286	2.3	.102
1209-2	–	128	179	1.45	2.49	148.8	±5.2	167	±21	44.08	2.0	0.0783	6.0	42.8	3.6	0.100	22	0.323	23	0.02335	3.6	.157
1209-3	–	79	59	0.76	1.56	158.5	±6.8	296	±53	43.8	2.6	0.067	17	40.2	4.4	0.131	21	0.449	21	0.0249	4.4	.205
1209-4	2.28	86	122	1.47	1.89	159.9	±4.3	178	±15	38.91	2.3	0.1163	7.1	39.8	2.7	0.099	14	0.344	15	0.02511	2.7	.186
1209-5	2.30	273	421	1.60	5.50	146.2	±3.2	141	±11	42.59	1.6	0.0778	3.9	43.60	2.2	0.060	22	0.189	22	0.02294	2.2	.103
1209-6	–	369	479	1.34	7.45	150.2	±2.2	164.1	±4.8	42.56	1.4	0.0780	6.0	42.43	1.5	0.0803	6.3	0.261	6.5	0.02357	1.5	.226
1209-7	32.96	310	317	1.06	9.51	152.5	±8.6	185	±63	28.00	2.7	0.335	7.4	41.8	5.7	0.083	64	0.28	64	0.0239	5.7	.089
1209-8	–	350	432	1.28	6.78	144.8	±2.2	140.1	±5.1	44.35	1.5	0.0556	4.1	44.02	1.5	0.0615	6.7	0.193	6.9	0.02272	1.5	.222
1209-9	4.86	120	138	1.19	2.53	149.4	±5.4	143	±26	40.59	2.0	0.105	12	42.7	3.6	0.068	40	0.219	40	0.02344	3.6	.091
1209-10	5.16	250	337	1.39	5.39	151.5	±3.7	159	±15	39.88	1.6	0.1178	6.6	42.0	2.5	0.078	22	0.257	22	0.02378	2.5	.114
1209-11	7.45	37	52	1.44	0.815	151	±14	167	±62	39.1	3.2	0.168	13	42.2	9.4	0.113	61	0.37	62	0.0237	9.4	.152
JWL1321																						
1321-1	2.84	109	118	1.11	2.20	145.0	±3.2	128	±10	42.71	2.1	0.0641	6.4	43.96	2.2	0.0413	19	0.129	19	0.02275	2.2	.116
1321-2	0.96	108	84	0.80	2.17	147.0	±3.1	165	±11	42.95	2.1	0.0790	8.0	43.37	2.2	0.0716	11	0.228	12	0.02306	2.2	.187
1321-3	–	272	332	1.26	5.25	144.1	±2.3	143.1	±4.7	44.52	1.6	0.0534	6.8	44.23	1.6	0.0585	6.2	0.183	6.4	0.02261	1.6	.249
1321-4	0.00	188	251	1.38	3.87	152.7	±3.4	148.0	±5.5	41.73	2.3	0.0595	6.0	41.73	2.3	0.0595	6.0	0.197	6.4	0.02396	2.3	.356
1321-5	1.83	195	313	1.66	4.00	149.3	±2.8	141.5	±6.3	41.91	1.8	0.0568	6.0	42.69	1.9	0.0422	15	0.136	15	0.02343	1.9	.129
1321-6	2.25	88	109	1.29	1.80	149.0	±3.6	143	±15	41.79	2.2	0.0691	6.3	42.8	2.4	0.0512	18	0.165	18	0.02339	2.4	.133
1321-7	5.05	56	88	1.62	1.11	139.3	±4.6	125	±14	43.5	2.7	0.0736	8.5	45.8	3.4	0.033	54	0.098	54	0.02184	3.4	.062
1321-8	3.22	42	59	1.44	0.877	148.6	±4.8	137	±14	41.5	3.0	0.109	9.6	42.9	3.3	0.085	18	0.273	18	0.02332	3.3	.181
1321-9	3.62	56	52	0.97	1.13	144.2	±5.6	145	±27	42.6	3.6	0.0798	8.9	44.2	3.9	0.051	30	0.159	30	0.02263	3.9	.131
1321-10	1.07	317	430	1.40	6.06	140.3	±2.2	129.4	±5.9	44.96	1.5	0.0603	4.4	45.44	1.6	0.0519	10	0.157	10	0.02200	1.6	.151
1321-11	0.36	278	430	1.60	5.45	144.7	±3.2	135.1	±4.5	43.88	2.2	0.0566	4.3	44.04	2.2	0.0537	5.7	0.168	6.2	0.02271	2.2	.362
1321-12	10.80	13	11	0.90	0.313	160	±15	158	±94	35.5	4.9	0.181	19	39.8	9.3	0.100	70	0.35	71	0.0251	9.3	.132
JWL1220																						
1220-1	–	107	154	1.49	2.20	159.0	±5.1	208	±20	41.81	2.0	0.1076	5.3	40.0	3.2	0.139	13	0.479	14	0.02498	3.2	.235
1220-2	0.37	448	269	0.62	9.33	154.0	±2.1	182.0	±8.3	41.22	1.3	0.0782	3.0	41.37	1.4	0.0753	5.2	0.251	5.3	0.02417	1.4	.262
1220-3	3.69	565	424	0.77	12.0	152.1	±2.5	168	±16	40.35	1.3	0.1003	3.8	41.89	1.7	0.0718	13	0.236	13	0.02387	1.7	.126
1220-4	7.19	772	467	0.62	17.0	151.1	±2.8	178	±24	39.12	1.2	0.1262	3.8	42.15	1.8	0.070	17	0.231	17	0.02372	1.8	.110
1220-5	6.82	616	718	1.20	13.0	146.5	±3.0	131	±13	40.55	1.5	0.1017	2.7	43.52	2.1	0.047	24	0.150	24	0.02298	2.1	.084
1220-6	10.47	290	371	1.32	6.44	147.5	±4.6	145	±22	38.68	1.7	0.149	10	43.2	3.2	0.067	40	0.215	40	0.02315	3.2	.080
1220-7	2.14	366	484	1.37	7.55	149.8	±3.5	145	±14	41.62	1.5	0.0810	3.2	42.53	2.3	0.064	23	0.208	23	0.02351	2.3	.103
1220-8	2.55	540	439	0.84	11.0	146.8	±2.4	134	±13	42.32	1.3	0.0715	4.6	43.42	1.7	0.0513	18	0.163	18	0.02303	1.7	.093
1220-9	14.84	418	308	0.76	9.66	146.1	±4.4	122	±40	37.16	1.3	0.174	6.1	43.6	3.1	0.057	44	0.180	44	0.02292	3.1	.069
1220-10	–	745	636	0.88	15.0	150.9	±2.3	158.7	±6.9	42.60	1.5	0.0628	2.6	42.23	1.5	0.0695	5.4	0.227	5.6	0.02368	1.5	.271
1220-11	10.38	395	262	0.69	8.57	144.5	±3.7	119	±35	39.54	1.4	0.1339	7.4	44.1	2.6	0.052	41	0.161	41	0.02267	2.6	.064

Errors are 1-sigma; Pb_c and Pb^* indicate the common and radiogenic portions, respectively.
Error in Standard calibration was 0.26% (not included in above errors but required when comparing data from different mounts).

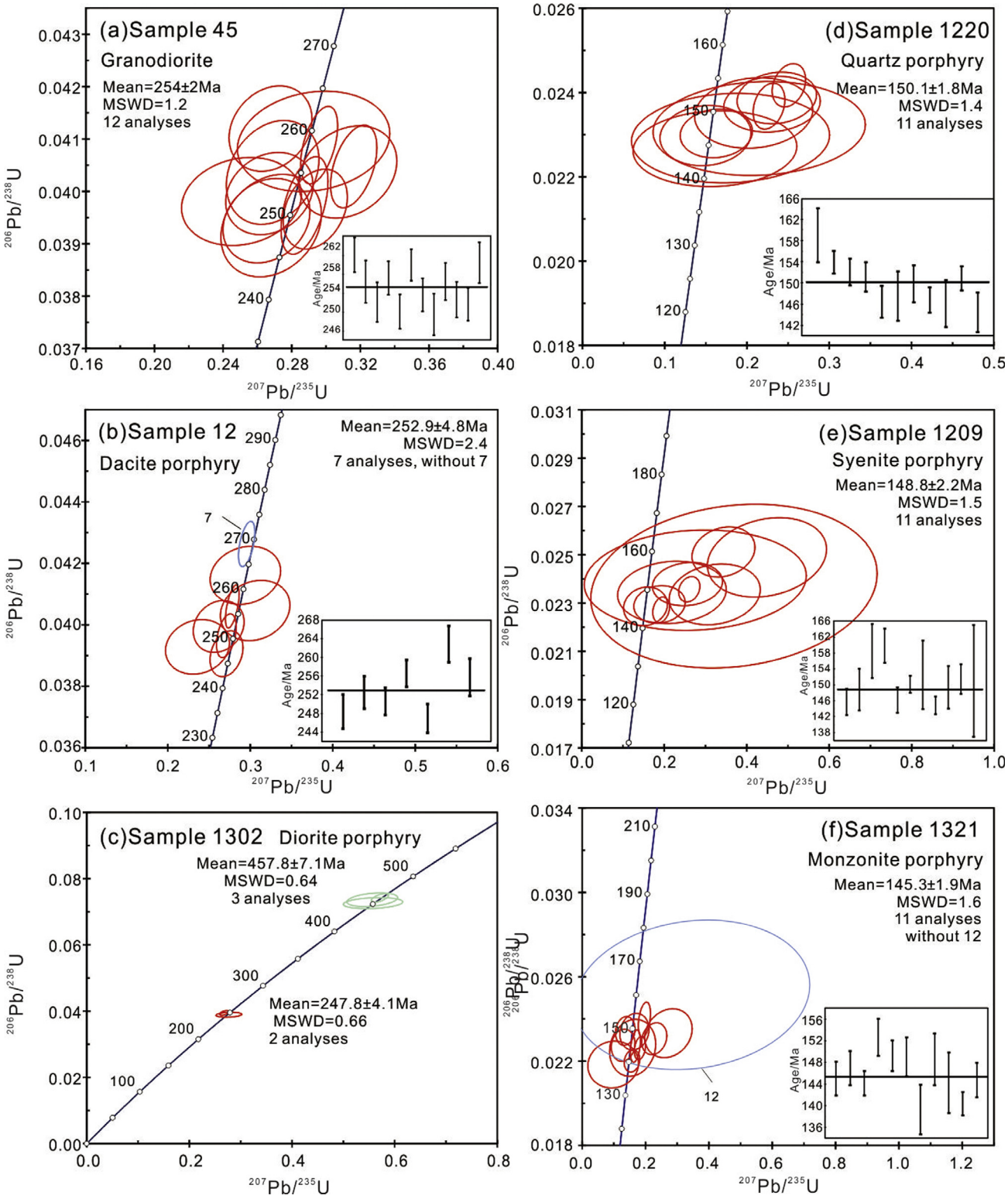

Fig. 12. Zircon U–Pb concordia diagrams of the different intrusions from the Jiawula deposit. (a) to (c) Late Permian to Early Triassic (Indosinian); (d) to (f) Late Jurassic (Yanshanian) intrusions.

intrusions in Jiawula, on the other hand, show model ages older than 1000 Ma, which indicates the presence of relatively older crust among the more juvenile crust in this area.

The intermediate-felsic rocks in the Great Xing'an Range falling close to the "mantle array" might have originated from mantle-derived magma and are consist with the tendency of the juvenile lower crust (Wu et al., 2003b). For the Jiawula deposit, the source of magma may have been sourced from the juvenile lower crust and the weakly enriched mantle. As part of circum Pacific tectonic domain and significant topographic boundary in east China, the Taihang-Great Xing'an Range tectonomagmatic belt is of great geological significance with the abrupt change in crustal thickness and

Table 8
Sr-Nd isotopic analyses for the intrusive rocks in the Jiawula deposit.

Sample No.	Rb (ppm)	Sr (ppm)	$(^{87}Rb/^{86}Sr)_m$	$(^{87}Sr/^{86}Sr)_m$	Sm (ppm)	Nd (ppm)	$(^{147}Sm/^{144}Nd)_m$	$(^{143}Nd/^{144}Nd)_m$	$(^{87}Sr/^{86}Sr)_i$	$(^{143}Nd/^{144}Nd)_i$	t (Ma)	ε_{Nd} (t)	T_{DM}	T_{2DM}	$f_{Sm/Nd}$
1220	346	83.6	11.9729	0.730767	6.15	36.4	0.1020	0.512372	0.70522	0.512272	150	-3.4	1064	1216	−0.48
1209	195	204	2.7736	0.711032	15.4	84.9	0.1098	0.512478	0.70520	0.512372	148	-1.5	988	1060	−0.44
1321	262	201	3.7688	0.712366	14.7	81.3	0.1096	0.512461	0.70458	0.512357	145	-1.8	1011	1087	−0.44
1302	55.7	560	0.2880	0.705663	6.6	34.4	0.1158	0.512496	0.70465	0.512308	248	-0.2	1021	1038	−0.41

Values with subscript m stand for measured values and those with i are initial.

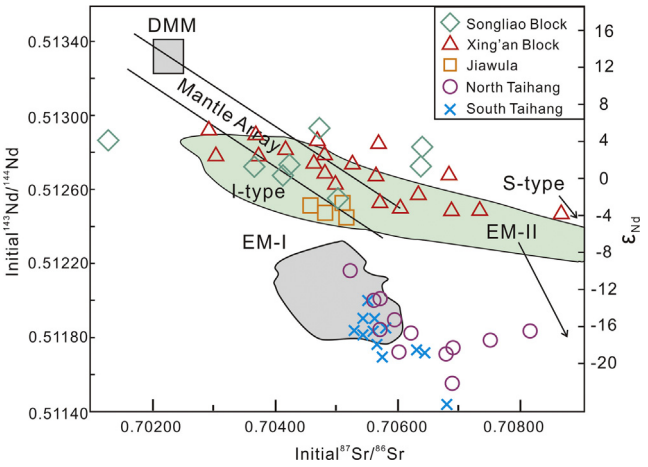

Fig. 13. Initial $^{143}Nd/^{144}Nd$ vs. initial $^{87}Sr/^{86}Sr$ correlation diagrams of Yanshanian intrusions from the Taihang Mountains, Great Xing'an Range and the Jiawula deposit. Data of Songliao Block and Xing'an Block are from Wu et al. (2003b); data of Taihang are from Cai et al. (2004). DMM: depleted MORB mantle; EM-I: enriched mantle I; EM-II: enriched mantle II. End-members are defined by Hart, 1984; Zindler and Hart, 1986; Wu et al., 2000, 2003b).

gravity anomaly, where Mesozoic magmatic activities widely occurred (Deng et al., 1996, 2004; Chen and Zhai, 2003; Luo et al., 2008). The source of magma in the Taihang Mountains might be related to materials from the EM-I enriched mantle reservoir. The involvement of the ancient lower crustal components in the North China Craton can be related to the Early Cretaceous lithosphere thinning and crust-mantle decoupling (Li and Santosh, 2014; Li et al., 2013, 2015, 2016). Thus, the characteristics of lithosphere mantle beneath the Taihang Mountains and the Great Xing'an Range are diverse within this important tectono-magmatic belt.

6.4. Implications of the magmatism on mineralization

The intrusions in the two episodes show a close spatial relationship with ore bodies in the Jiawula deposit (Fig. 1c). Nevertheless, the ca. 254 Ma–247 Ma intrusions did not contribute to mineralization in Jiawula because of the nearly 100 Ma gap between emplacement and mineralization. On the other hand, the intermediate to felsic hypabyssal intrusions formed at ca. 150 Ma–145 Ma just before Pb-Zn mineralization at 142.7 ± 1.3 Ma (Li et al., 2014b). Thus, the Late Jurassic magmatic event presents very close spatio-temporal relationship to the mineralization in Jiawula.

If we compare the two magmatic episodes, they can provide us helpful clues on the mineralization significance of the magmatism. As for the series of the granitoids, the ca. 150 Ma–145 Ma intrusions show more transitional geochemical features between I-type and A-type than the ca. 254 Ma–247 Ma granitoids although both of them are classified as I-type. These transitional features during late Jurassic can be explained by the reactivation of lower-most crust which happened in eastern China during Yanshanian with Mesozoic metallogenic explosion in east China (Mao et al., 2003; Pirajno et al., 2009; Li et al., 2014a,c). The Yanshanian intrusions show more striking negative anomaly in Eu, Sr, P, and Ti in the spidergrams (Fig. 6b), which suggests a stronger fractionation processes of plagioclase, K-feldspar, apatite, rutile, etc. during Late Jurassic. Another remarkable point is that barium is moderately depleted in the Yanshanian intrusions, which might be due to the behavior of this element in K-feldspar (Mittlefehldt and Miller, 1983; Bonin, 1990) and can be regarded as additional evidence for stronger fractionation during late Jurassic.

According to the classification of Nachit et al. (2005), the biotite in diorite porphyry (247.8 ± 4.1 Ma) crystallized as a primary magmatic mineral whereas biotite re-equilibration took place in the monzonite (145.3 ± 1.9 Ma) and syenite porphyry (148.8 ± 2.2 Ma) (Fig. 8b). It is proposed that for the phenocrysts in feldspar porphyry during the ca. 150 Ma–145 Ma magmatic event, re-equilibration might have happened between the late-magmatic and hydrothermal stages. The results of the two-feldspar geothermometry, the temperature gap from about 600–470 °C provides additional evidence of this re-equilibration event, which might represent the beginning of the alteration process prior to the mineralization.

The hornblende in monzonite porphyry and diorite porphyry crystallized at early stage at a high temperature (830–900 °C) (Fig. 10a). The oxygen fugacity calculated from the hornblende in monzonite porphyry and diorite porphyry differs distinctly (Fig. 10b). A high oxygen fugacity is thought to be favorable for the transport of some metals from magma to ore-forming fluid (Mungall, 2002; Sun et al., 2013, 2015). The oxygen fugacity appears to be higher in the monzonite porphyry (145.3 ± 1.9 Ma) than that in diorite porphyry (247.8 ± 4.1 Ma), which supports the preference of relatively higher oxygen fugacity for Pb-Zn mineralization in Jiawula.

The quartz porphyry (emplaced at 150.1 ± 1.8 Ma) is slightly older than the 142.7 ± 1.3 Ma mineralization event and shows quartz crystallization temperatures of ranging between 850 and 600 °C with most temperatures in the 750–600 °C interval. This temperature range is more constrained than that of the 145.3 ± 1.9 Ma monzonite porphyry, which has the closest temporal relationship with the mineralization and shows two temperature intervals for feldspar crystallization: 450–395 °C and 830–623 °C. This temperature gradient may have been favorable for metal precipitation (Heinrich et al., 1999; Zhao et al., 2014).

7. Conclusions

(1) Two magmatic episodes are recorded in the Jiawula deposit. The ca. 254–247 Ma intrusions are composed of granodiorite (254 ± 2 Ma), dacite porphyry (252.9 ± 4.8 Ma), and diorite porphyry (278 ± 4.1 Ma), while the ca.150–145 Ma granitoids are made up of quartz porphyry (150.1 ± 1.8 Ma), syenite porphyry (148.8 ± 2.2 Ma), and monzonite porphyry (145.3 ± 1.9 Ma). The metallogenic event is slightly younger than this Late Jurassic magmatic event.

(2) The two magmatic events in Jiawula are fractionated I-type granitoids and originated from juvenile lower crust and weakly enriched mantle. The ca. 254–247 Ma magmatic episode in Jiawula is associated with the southward subduction of the Mongol-Okhotsk oceanic plate, and the I-type characteristics indicate an active continental margin setting. The ca. 150–145 Ma magmatic episode occurred after the closure of the Mongol-Okhotsk Ocean and before large-scale delamination of the thickened continental crust.

(3) Comparison of the intrusions in the Jiawula deposit with regards to crystallization temperatures, fractionation, and oxygen fugacity shows that Pb-Zn mineralization is closely related with high oxygen fugacities and decreasing temperatures, which are most likely associated with the magmatic-hydrothermal transition.

Acknowledgements

We are grateful to Derong Gao, Mengjie Shan and Yixiang Lan for the assistance during fieldwork. Anonymous reviewers and editors are sincerely thanked for the comments which greatly improved this manuscript. Funding for this project was granted by National Key Research and Development Program of China (2016YFC0600106), China Geological Survey (12120114051101), Ministry of Land and Resources (201411024-4), Ministry of Education of China (20130022110003), and the Fundamental Research Funds for the Central Universities (35732015067). This study was jointly funded by the China Scholarship Council.

References

Bai, L.A., Sun, J.G., Gu, A.L., Zhao, K.Q., Sun, Q.L., 2014. A review of the genesis, geochronology, and geological significance of hydrothermal copper and associated metals deposits in the Great Xing'an Range, NE China. Ore Geol. Rev. 61, 192–203.

Benisek, A., Dachs, E., Kroll, H., 2010. A ternary feldspar-mixing model based on calorimetric data: development and application. Contrib. Miner. Petrol. 160, 327–337.

Bonin, B., 1990. From orogenic to anorogenic settings: evolution of granitoid suites after a major orogenesis. Geol. J. 25, 261–270.

Boynton, W.V., 1984. Geochemistry of the rare earth elements: Meteorite studies. In: Henderson, P. (Ed.), Rare Earth Element Geochemistry. Elsevier, Amsterdam, pp. 63–114.

Cai, J.H., Yan, G.H., Xiao, C.D., Wang, G.Y., Mu, B.L., Zhang, R.H., 2004. Nd, Sr, Pb isotopic characteristics of the Mesozoic intrusive rocks in the Taihang-Da Hinggan Mountains Tectonomagmatic Belt and their source region. Acta Petrol. Sin. 20, 1225–1242 (in Chinese with English Abstract).

Chen, B., Zhai, M.G., 2003. Geochemistry of late Mesozoic lamprophyre dykes from the Taihang Mountains, north China, and implications for the sub-continental lithospheric mantle. Geol. Mag. 140, 87–93.

Chen, Y.J., Zhang, C., Li, N., Yang, Y.F., Deng, K., 2012. Geology of the Mo deposits in Northeast China. J. Jilin Univ. (Earth Science Edition) 42, 1223–1268 (in Chinese with English abstract).

Deer, W.A., Howie, R.A., Zussman, J., 1992. An Introduction to the Rock Forming Minerals. Longman, London, p. 696.

Deng, J.F., Mo, X.X., Zhao, H.L., Wu, Z.X., Luo, Z.H., Su, S.G., 2004. A new model for the dynamic evolution of Chinese lithosphere: 'continental roots-plume tectonics'. Earth Sci. Rev. 65, 223–275.

Deng, J.F., Zhao, H.L., Mo, X.X., Wu, Z.X., Luo, Z.H., 1996. Continental Roots-Plume Tectonics of China: Key to the Continental Dynamics. Geological Publishing House, Beijing. 1-110 (in Chinese with English Abstract).

Elkins, L.T., Grove, T.L., 1990. Ternary feldspar experiments and thermodynamic models. Am. Mineral. 75, 544–559.

Foster, M.D., 1961. Shorter contributions to general geology interpretation of the composition of trioctahedral micas. Geological Survey Professional Paper 354, 11.

Ge, W.C., Wu, F.Y., Zhou, C.Y., Abdel Rahman, A.A., 2005. Emplacement age of the Tahe granite and its constraints on the tectonic nature of the Ergun block in the northern part of the Da Hinggan Range. Chin. Sci. Bull.-English Edition 50, 2097–2105.

Geng, W.H., 2006. Mesozoic Subvolcanic Cu-Ag Polymetallic Deposits in East China. Press of Metallurgy Industry, Beijing. 1-159 (in Chinese with English Abstract).

Ghiorso, M.S., 1984. Activity/composition relations in the ternary feldspars. Contrib. Miner. Petrol. 87, 282–296.

Guo, P., Santosh, M., Li, S.R., Li, Q., 2014. Crustal evolution in the central part of Eastern NCC: Zircon U–Pb ages from multiple magmatic pulses in the Luxi area and implications for gold mineralization. Ore Geol. Rev. 60, 126–145.

Hart, S.R., 1984. A large-scale isotope anomaly in the Southern Hemisphere mantle. Nature 309, 753–757.

Heinrich, C.A., Günther, D., Audétat, A., Ulrich, T., Frischknecht, R., 1999. Metal fractionation between magmatic brine and vapor, determined by microanalysis of fluid inclusions. Geology 27, 755–758.

Hora, J.M., Kronz, A., Möller-McNett, S., Wörner, G., 2013. An Excel-based tool for evaluating and visualizing geothermobarometry data. Comput. Geosci. 56, 178–185.

Jahn, B.M., Wu, F.Y., Capdevila, R., Martineau, F., Zhao, Z.H., Wang, Y.X., 2001. Highly evolved juvenile granites with tetrad REE patterns: the Woduhe and Baerzhe granites from the Great Xing'an Mountains in NE China. Lithos 59, 171–198.

King, P.L., White, A.J.R., Chappell, B.W., Allen, C.M., 1997. Characterization and origin of aluminous A-type granites from the Lachlan Fold Belt, southeastern Australia. J. Petrol. 38, 371–391.

Kravchinsky, V.A., Cogne, J.P., Harbert, W.P., Kuzmin, M.I., 2002. Evolution of the Mongol-Okhotsk Ocean as constrained by new palaeomagnetic data from the Mongol-Okhotsk suture zone, Siberia. Geophys. J. Int. 148, 34–57.

Leake, B.E., Woolley, A.R., Arps, C.E.S., 1997. Nomenclature of amphiboles: report of the subcommittee on amphiboles of the International Mineralogical Association, commission on new minerals and mineral names. Can. Mineral. 35, 219–246.

Li, L., Li, S.R., Santosh, M., Li, Q., Gu, Y., Lü, W.J., Zhang, H.F., Shen, J.F., Zhao, G.C., 2016. Dyke swarms and their role in the genesis of world-class gold deposits: Insights from the Jiaodong peninsula, China. J. Asian Earth Sci. http://dx.doi.org/10.1016/j.jseaes.2016.06.015.

Li, L., Santosh, M., Li, S.R., 2015. The 'Jiaodong type gold deposits: characteristics, origin and prospecting. Ore Geol. Rev. 65, 589–611.

Li, Q., Santosh, M., Li, S.R., Guo, P., 2014a. The formation and rejuvenation of continental crust in the central North China Craton: Evidence from zircon U-Pb geochronology and Hf isotope. J. Asian Earth Sci. 95, 17–32.

Li, S.R., Santosh, M., 2014. Metallogeny and craton destruction: records from the North China Craton. Ore Geol. Rev. 56, 376–414.

Li, S.R., Santosh, M., Zhang, H.F., Luo, J.Y., Zhang, J.Q., Li, C.L., Song, J.Y., Zhang, X.B., 2014b. Metallogeny in response to lithospheric thinning and craton destruction: geochemistry and U-Pb zircon chronology of the Yixingzhai gold deposit, central North China Craton. Ore Geol. Rev. 56, 457–471.

Li, S.R., Santosh, M., Zhang, H.F., Shen, J.F., Dong, G.C., Wang, J.Z., Zhang, J.Q., 2013. In homogeneous lithospheric thinning in the central North China Craton: Zircon U-Pb and S-He-Ar isotopic record from magmatism and metallogeny in the Taihang Mountains. Gondwana Res. 23, 141–160.

Li, T.G., Wu, G., Liu, J., Hu, Y.Q., Zhang, Y.F., Luo, D.F., 2014c. Rb-Sr isochron age of the Jiawula Ag-Pb-Zn deposit in the Manzhouli area and its geological significance. Acta Petrol. Sin. 30, 257–270 (in Chinese with English abstract).

Lin, Q., Ge, W.C., Wu, F.Y., Sun, D.Y., Cao, L., 2004. Geochemistry of Mesozoic granites in Da Hinggan Ling ranges. Acta Petrol. Sin. 20, 403–412.

Liu, J.M., Zhang, R., Zhang, Q.Z., 2004. The regional metallogeny of Da Hinggan Ling, China. Earth Sci. Front. 11, 269–277 (In Chinese with English abstract).

Liu, J., Mao, J.W., Wu, G., Wang, F., Luo, D.F., Hu, Y.B., 2014. Zircon U-Pb and molybdenite Re-Os dating of the Chalukou porphyry Mo deposit in the northern Great Xing'an range, China and its geological significance. J. Asian Earth Sci. 79, 696–709.

Luo, Z.H., Lu, X.X., Guo, S.F., Sun, J., Chen, B.H., Huang, F., Yang, Z.F., 2008. Metallogenic systems on the transmagmatic fluid theory. Acta Petrol. Sin. 24, 2669–2678 (In Chinese with English abstract).

Mao, J.W., Wang, Y.T., Zhang, Z.H., Yu, J.J., Niu, B.G., 2003. Geodynamic settings of Mesozoic large-scale mineralization in North China adjacent areas. Sci. China (Series D) 46, 838–851.

Mao, J.W., Xie, G.Q., Zhang, Z.H., Li, X.F., Wang, Y.T., Zhang, C.Q., Li, Y.F., 2005. Mesozoic large-scale metallogenic pulses in North China and corresponding geodynamic settings. Acta Petrol. Sin. 21, 169–188 (In Chinese with English abstract).

Mao, J.W., Zhou, Z.H., Wu, G., Jiang, S.H., Liu, C.L., Li, H.M., Ouyang, H.G., Liu, J., 2013. Metallogenic regularity and minerogenetic series of ore deposits in Inner Mongolia and adjacent areas. Mineral Deposits 32, 715–729 (in Chinese with English abstract).

Maruyama, S., Isozaki, Y., Kimura, G., Terabayashi, M., 1997. Paleogeographic maps of the Japanese Islands: Plate tectonic synthesis from 750 Ma to the present. Isl. Arc 6, 121–142.

Meng, E., Xu, W.L., Pei, F.P., Yang, D.B., Wang, F., Zhang, X.Z., 2011. Permian bimodal volcanism in the Zhangguangcai Range of eastern Heilongjiang Province, NE China: zircon U-Pb-Hf isotopes and geochemical evidence. J. Asian Earth Sci. 41, 119–132.

Meng, Q.R., 2003. What drove late Mesozoic extension of the northern China-Mongolia tract? Tectonophysics 369, 155–174.

Mittlefehldt, D.W., Miller, C.F., 1983. Geochemistry of the Sweetwater Wash Pluton, California: implications for "anomalous" trace element behavior during differentiation of felsic magmas. Geochim. Cosmochim. Acta 47, 109–124.

Mungall, J.E., 2002. Roasting themantle: slabmelting and the genesis of major Au and Au-rich Cu deposits. Geology 30, 915–918.

Nachit, H., Ibhi, A., Abia, E.H., Ohoud, M.B., 2005. Discrimination between primary magmatic biotites, reequilibrated biotites and neoformed biotites. C.R. Geosci. 337, 1415–1420.

Nie, F.J., Li, Q.F., Liu, C.H., Ding, C.W., 2015. Geology and origin of Ag-Pb-Zn deposits occurring in the Ulaan-Jiawula metallogenic province, northeast Asia. J. Asian Earth Sci. 97, 424–441.
Niu, S.D., Li, S.R., Santosh, M., Zhang, D.H., Li, Z.D., Shan, M.J., Gao, D.R., Zhao, W.B., 2016. Mineralogical and isotopic studies of base metal sulfides from the Jiawula Ag-Pb-Zn deposit, Inner Mongolia, NE China. J. Asian Earth Sci. 115, 480–491.
Ouyang, H.G., Mao, J.W., Santosh, M., Zhou, J., Zhou, Z.H., Wu, Y., Hou, L., 2013. Geodynamic setting of Mesozoic magmatism in NE China and surrounding regions: perspectives from spatio-temporal distribution patterns of ore deposits. J. Asian Earth Sci. 78, 222–236.
Pan, L.J., Sun, E.S., 1992. Geological characteristics of the Jiawula silver-lead-zinc deposit, Inner Mongolia. Mineral Deposits 11, 45–53 (in Chinese with English abstract).
Pirajno, F., 2012. The Geology and Tectonic Settings of China's Mineral Deposits. Springer Science & Business Media. 249–380.
Pirajno, F., Ernst, R.E., Borisenko, A.S., Fedoseev, G., Naumov, E.A., 2009. Intraplate magmatism in Central Asia and China and associated metallogeny. Ore Geol. Rev. 35, 114–136.
Porter, T.M., 2016. The geology, structure and mineralisation of the Oyu Tolgoi porphyry copper-gold-molybdenum deposits, Mongolia: a review. Geosci. Front. 7, 375–407.
Putirka, K.D., 2008. Thermometers and barometers for volcanic systems. Rev. Mineral. Geochem. 69, 61–120.
Qin, K.Z., Tanaka, R., Ishihara, S., Meng, Z. J., 1996. K-Ar, Rb-Sr isochorn and single U-Pb ages and their significance of volcanic intrusive complex in Jiawula-Chagan Ag-Pb-Zn orefield, NE-Inner Mongolia. In: Proceedings of the international symposium on the geologic and metallogenic correlation in the junction area among China, Russia and Mongolia, June 11–13, Manzhouli, pp. 83–85.
Qin, K.Z., Tanaka, R., Li, W.S., Ishihara, S., 1998. The discovery of Indosinian Granites in Manzhouli Area: evidence from Rb-Sr Isochrons. Acta Petrol. Mineral. 3, 235–240 (in Chinese with English abstract).
Ridolfi, F., Puerini, M., Renzulli, A., Menna, M., Toulkeridis, T., 2008. The magmatic feeding system of El Reventador volcano (Sub-Andean zone, Ecuador) constrained by texture, mineralogy and thermobarometry of the erupted products. J. Volcanol. Geoth. Res. 176, 94–106.
Ridolfi, F., Renzulli, A., Puerini, M., 2010. Stability and chemical equilibrium of amphibole in calc-alkaline magmas: an overview, new thermobarometric formulations and application to subduction-related volcanoes. Contrib. Miner. Petrol. 160, 45–66.
Scaillet, B., Evans, B.W., 1999. The 15 June 1991 eruption of Mount Pinatubo; I, Phase equilibria and pre-eruption P-T–fO2–fH2 conditions of the dacite magmas. J. Petrol. 40, 381–411.
She, H.Q., Li, J.W., Xiang, A.P., Guan, J.D., Yang, X.C., Zhang, D.Q., Tan, G., Zhang, B., 2012. U-Pb ages of the zircons from primary rocks in middle-northern Daxinganling and its implications to geotectonic evolution. Acta Petrol. Sin. 28, 571–594 (in Chinese with English abstract).
Sun, S.S., McDonough, W.F., 1989. Chemical and isotopic systematics of oceanic basalts: Implications for mantle composition and processes. In: Saunders, A.D., Norry, M.J. (Eds.), Magmatism in Ocean Basins. Geological Society of Special Publication, London, pp. 313–345.
Sun, W.Y., Li, S.R., Santosh, M., Wang, X., Zhang, L.J., 2014. Isotope geochemistry and geochronology of the Qiubudong silver deposit, central North China Craton: implications for ore genesis and lithospheric dynamics. Ore Geol. Rev. 57, 229–242.
Sun, W.D., Huang, R.F., Li, H., Hua, Y.B., Zhang, C.C., Sun, S.J., Zhang, L.P., Ding, Xing., Li, C.Y., Robert, E.Z., Ling, M.X., 2015. Porphyry deposits and oxidized magmas. Ore Geol. Rev. 65, 97–131.
Sun, W.D., Liang, H.Y., Ling, M.X., Zhan, M.Z., Ding, X., Zhang, H., Yang, X.Y., Li, Y.L., Ireland, T.R., Wei, Q.R., Fan, W.M., 2013. The link between reduced porphyry copper deposits and oxidized magmas. Geochim. Cosmochim. Acta 103, 263–275.
Sylvester, P.J., 1998. Postcollisional strongly peraluminous granites. Lithos 45, 29–44.
Tang, J., Xu, W.L., Wang, F., Wang, W., Xu, M.J., Zhang, Y.H., 2014. Geochronology and geochemistry of Early-Middle Triassic magmatism in the Erguna Massif, NE China: constraints on the tectonic evolution of the Mongol-Okhotsk Ocean. Lithos 184, 1–16.
Tang, J., Xu, W.L., Wang, F., Zhao, S., Wang, W., 2016. Early Mesozoic southward subduction history of the Mongol-Okhotsk oceanic plate: evidence from geochronology and geochemistry of Early Mesozoic intrusive rocks in the Erguna Massif, NE China. Gondwana Res. 31, 218–240.
Tang, Y.J., Zhang, H.F., Ying, J.F., Su, B.X., Chu, Z.Y., Xiao, Y., Zhao, X.M., 2013. Highly heterogeneous lithospheric mantle beneath the Central Zone of the North China Craton evolved from Archean mantle through diverse melt refertilization. Gondwana Res. 23, 130–140.
Tomurtogoo, O., Windley, B.F., Kroner, A., Badarch, G., Liu, D.Y., 2005. Zircon age and occurrence of the Adaatsag ophiolite and Muron shear zone, central Mongolia: constraints on the evolution of the Mongol-Okhotsk ocean, suture and orogen. J. Geol. Soc. London 162, 125–134.
Wang, D.H., Zheng, Z.H., Chen, Y.C., Tang, J.X., Li, J.K., Ying, L.J., 2010. New data of the Rock-Forming and Ore-forming Chronology for China's important mineral resources areas. Acta Geol. Sinica 84, 1030–1040 (in Chinese with English abstract).
Wang, F., Zhou, X.H., Zhang, L.C., Ying, J.F., Zhang, Y.T., Wu, F.Y., Zhu, R.X., 2006. Late Mesozoic volcanism in the Great Xing'an Range (NE China): timing and implications for the dynamic setting of NE Asia. Earth Planet. Sci. Lett. 251, 179–198.
Wang, T., Guo, L., Zhang, L., Yang, Q., Z, Zhang, J., Tong, Y., Ye, K., 2015. Timing and evolution of Jurassic-Cretaceous granitoid magmatisms in the Mongol-Okhotsk belt and adjacent areas, NE Asia: Implications for transition from contractional crustal thickening to extensional thinning and geodynamic settings. J. Asian Earth Sci. 97, Part B, 365–392.
Wark, D.A., Watson, E.B., 2006. TitaniQ: a titanium-in-quartz geothermometer. Contrib. Miner. Petrol. 152, 743–754.
Whalen, J.B., Currie, K.L., Chappell, B.W., 1987. A-type granites: geochemical characteristics, discrimination and petrogenesis. Contrib. Miner. Petrol. 95, 407–419.
Wu, F.Y., Jahn, B.M., Wilde, S.A., Lo, C.H., Yui, T.F., Lin, Q., Sun, D.Y., 2003a. Highly fractionated I-type granites in NE China (I): geochronology and petrogenesis. Lithos 66, 241–273.
Wu, F.Y., Jahn, B.M., Wilde, S.A., Lo, C.H., Yui, T.F., Lin, Q., Sun, D.Y., 2003b. Highly fractionated I-type granites in NE China (II): isotopic geochemistry and implications for crustal growth in the Phanerozoic. Lithos 67, 191–204.
Wu, F.Y., Jahn, B.M., Wilde, S., Sun, D.Y., 2000. Phanerozoic crustal growth: U-Pb and Sr-Nd isotopic evidence from the granites in northeastern China. Tectonophysics 328, 89–113.
Wu, F.Y., Lin, J.Q., Wilde, A., Zhang, X.O., Yang, J.H., 2005. Nature and significance of the Early Cretaceous giant igneous event in eastern China. Earth Planet. Sci. Lett. 233, 103–119.
Wu, F.Y., Sun, D.Y., Ge, W.C., Zhang, Y.B., Grant, M.L., Wilde, S.A., Jahn, B.M., 2011. Geochronology of the Phanerozoic granitoids in northeastern China. J. Asian Earth Sci. 41, 1–30.
Wu, F.Y., Sun, D.Y., Li, H.M., Jahn, B.M., Wilde, S., 2002. A-type granites in northeastern China: age and geochemical constraints on their petrogenesis. Chem. Geol. 187, 143–173.
Wu, G., Sun, F.Y., Zhu, Q., Li, Z.T., Ding, Q.F., Li, G.Y., Pang, Q.B., Wang, H.B., 2006. Geological characteristics and genesis of gold deposits in Upper Heilongjiang Basin. Mineral Deposits 25, 215–230 (in Chinese with English abstract).
Xiao, W., Windley, B.F., Hao, J., Zhai, M.G., 2003. Accretion leading to collision and the Permian Solonker suture, Inner Mongolia, China: termination of the central Asian orogenic belt. Tectonics 22, 1–19.
Xiao, W.J., Sun, M., Santosh, M., 2015. Continental reconstruction and metallogeny of the Circum-Junggar areas and termination of the southern Central Asian Orogenic Belt. Geosci. Front. 6, 137–140.
Xu, W.L., Ji, W.Q., Pei, F.P., Meng, E., Yu, Y., Yang, D.B., Zhang, X.Z., 2009. Triassic volcanism in eastern Heilongjiang and Jilin Provinces, NE China: chronology, geochemistry, and tectonic implications. J. Asian Earth Sci. 34, 392–402.
Yang, Y.T., Guo, Z.X., Song, C.C., Li, X.B., He, S., 2015. A short-lived but significant Mongol-Okhotsk collisional orogeny in latest Jurassic–earliest Cretaceous. Gondwana Res. 28, 1096–1116.
Zhai, D.G., Liu, J.J., Wang, J.P., Yao, M.J., Wu, S.H., Fu, C., Liu, Z.J., Wang, S.G., Li, Y.X., 2013. Fluid evolution of the Jiawula Ag-Pb-Zn deposit, Inner Mongolia: mineralogical, fluid inclusion, and stable isotopic evidence. Int. Geol. Rev. 55, 204–224.
Zhai, D.G., Liu, J.J., Yang, Y.Q., Wang, J.P., Ding, L., Liu, X.W., Zhang, H.Y., 2012. Petrogenetic and metallogentic ages and tectonic setting of the Huangganglang Fe-Sn deposit, Inner Mongolia. Acta Petrol. Mineral. 31, 513–523 (in Chinese with English abstract).
Zhang, F.Q., Chen, H.L., Yu, X., Dong, C.W., Yang, S.F., Pang, Y.M., Batt, G.E., 2011. Early Cretaceous volcanism in the northern Songliao Basin, NE China, and its geodynamic implication. Gondwana Res. 19, 163–176.
Zhang, J.H., Gao, S., Ge, W.C., Wu, F.Y., Yang, J.H., Wilde, S.A., Li, M., 2010. Geochronology of the Mesozoic volcanic rocks in the Great Xing'an range, northeastern China: Implications for subduction-induced delamination. Chem. Geol. 276, 144–165.
Zhang, J.Q., Li, S.R., Santosh, M., Li, Q., Niu, S.D., Li, Z.D., Zhang, X.G., Jia, L.B., 2015a. Timing and origin of Mesozoic magmatism and metallogeny in the Wutai-Hengshan region: implications for destruction of the North China Craton. J. Asian Earth Sci. 113, 677–694.
Zhang, J.Q., Li, S.R., Santosh, M., Wang, J.Z., Li, Q., 2015b. Mineral chemistry of high-Mg diorites and skarn in the Han-Xing Iron deposits of South Taihang Mountains, China: constraints on mineralization process. Ore Geol. Rev. 64, 200–214.
Zhang, Y.P., Tang, K.D., 1989. Pre-Jurassic tectonic evolution of intercontinental region and the suture zone between the North China and Siberian platforms. J. SE Asian Earth Sci. 3, 47–55.
Zhao, B., Zhang, D.H., Shi, C.L., Zhang, R.Z., 2014. Rethinking of the metallogenic specialization and ore-bearing potential of redox-related granitoid. Acta Petrol. Miner. 33, 955–964 (in Chinese with English abstract).
Zheng, Y.F., Xiao, W.J., Zhao, G., 2013. Introduction to tectonics of China. Gondwana Res. 23, 1189–1206.
Zhou, J.B., Wilde, S.A., Zhang, X.Z., Zhao, G.C., Zheng, C.Q., Wang, Y.J., Zhang, X.H., 2009. The onset of Pacific margin accretion in NE China: evidence from the Heilongjiang high-pressure metamorphic belt. Tectonophysics 478, 230–246.
Zhou, Z.H., Lv, L.S., Feng, J.R., Li, C., Li, T., 2010. Molybdenite Re-Os ages of Huanggang skarn Sn–Fe deposit and their geological significance, Inner Mongolia. Acta Petrol. Sin. 26, 667–679 (in Chinese with English abstract).
Zhou, Z.H., Mao, J.W., Lyckberg, P., 2012. Geochronology and isotopic geochemistry of the A-type granites from the Huanggang Sn-Fe deposit, southern Great Hinggan Range, NE China: implication for their origin and tectonic setting. J. Asian Earth Sci. 49, 272–286.

Zhou, Z., Mao, J., Liu, J., Ouyang, H., Che, H., Ma, X., 2015. Early Cretaceous magmatism and ore mineralization in Northeast China: examples from Taolaituo Mo and Aobaotu Pb-Zn deposits. Int. Geol. Rev. 57, 229–256.

Zhu, D.C., Mo, X.X., Wang, L.Q., Zhao, Z.D., Niu, Y.L., Zhou, C.Y., Yang, Y.H., 2009. Petrogenesis of highly fractionated I-type granites in the Zayu area of eastern Gangdese, Tibet: constraints from zircon U-Pb geochronology, geochemistry and Sr-Nd-Hf isotopes. Sci. China, Ser. D Earth Sci. 52, 1223–1239 (in Chinese with English abstract).

Zindler, A., Hart, S.R., 1986. Chemical geodynamics. Annu. Rev. Earth Planet. Sci. 14, 493–557.